Petroleum Science 23 (2026) 5234–5251

Contents lists available at ScienceDirect

Petroleum Science

journal homepage: www.keaipublishing.com/en/journals/petroleum-science

Original Paper

Geological fault identification *via* multi-knowledge causally embedding graph representation applied in underground gas storage

Feng-Yuan Zhang [a,b], Ji-Zhou Tang [a,b,*], Hong-Liang Wu [c], Jie Liu [d], Jun Zhou [e], Shi-Jie Zhao [a,b], Fa-Mu Huang [f], Juan Zhang [e], Hao Wang [c], Jun-Lun Li [g]

[a] School of Ocean and Earth Science, Tongji University, Shanghai, 200092, China
[b] Shanghai Key Laboratory of Submarine Resources, Tongji University, Shanghai, 200092, China
[c] Research Institute of Petroleum Exploration and Development, PetroChina, Beijing, 100083, China
[d] School of Civil and Hydraulic Engineering, Huazhong University of Science and Technology, Wuhan, 430074, Hubei, China
[e] China National Logging Corporation, Xi'an, 710075, Shaanxi, China
[f] China Oil & Gas Pipeline Network Corporation, Shanghai, 200092, China
[g] School of Earth and Space Sciences, University of Science and Technology of China, Hefei, 230026, Anhui, China

A R T I C L E I N F O

Article history:
Received 7 July 2025
Received in revised form
11 November 2025
Accepted 27 May 2026
Available online 1 June 2026

Edited by Min Li

Keywords:
Geological reliability assessment
Fault identification
Structural causal modeling
Seismic exploration
Graph representation learning
Gas storage

A B S T R A C T

Geological fault identification is critical for gas storage safety, yet remains reliant on manual interpretation with inherent inefficiencies. While Artificial intelligent (AI) methods offer alternatives, their neglect of causal structures particularly physical mechanisms and geological confounders and severely limits sensitivity to subtle seismic signals. To overcome this, a multi-knowledge causally embedded graph representation approach for fault identification (FI) in seismic images is proposed. Utilizing geological prior knowledge, the seismic volume is first discretized into node sets through pixel-to-node transformation. To explicitly capture causal structures, a multi-relational feature computation method integrates: (a) spatial continuity constraints of faults as physical causality priors, and (b) seismic signal characteristics. Guided by these causal priors, Causally chain-graphs (CCGs) are constructed through knowledge-driven edge pruning and reinforcement, with connections constrained by pixel spatial receptive fields to reflect geological causality. These causally structured graphs subsequently undergo feature aggregation *via* graph convolutions, modeling non-Euclidean relationships between nodes. The pipeline evolves from low-level graphs to high-order fault representations, enabling end-to-end pixel-level identification. A gas storage plot in central China was used to verify the effectiveness of the proposed method, and the graph representation learning framework demonstrates excellent performance in pixel-level fault identification within complex geological structures. It efficiently detects the NE-SW trending fault system, including regional, block-bounding, and minor intra-block faults, achieving a mean accuracy of 93.11% and an average F1-score of 0.758. The framework significantly enhances the detection capability and noise immunity for subtle deep-seated faults (with amplitude variations <5%). It provides intelligent early-warning analysis for critical issues in gas storage operations, such as late-stage tectonic reactivation, compromised caprock integrity due to gently dipping boundary faults, and reservoir heterogeneity exacerbated by fault interactions.

1. Introduction

Achieving carbon neutrality has emerged as a global consensus for addressing escalating climate challenges (Liu et al., 2022; Zhang et al., 2025b), driving heightened research interest in sustainable energy solutions (Jaiswal et al., 2022). The safety and stability of underground gas storage (UGS) facilities constitute critical infrastructure elements for maintaining natural gas

* Corresponding author.
E-mail address: jeremytang@tongji.edu.cn (J.-Z. Tang).
Peer review under the responsibility of China University of Petroleum (Beijing).

https://doi.org/10.1016/j.petsci.2026.05.047
1995-8226/

supply-demand equilibrium and ensuring energy security (Li et al., 2021). Site selection rationality for UGS facilities requires meticulous evaluation of geological faults-structural discontinuities formed by crustal stress-induced rock fracturing, characterized by measurable displacement along fracture planes (Xiong et al., 2018).

Conventional geological fault identification (FI) predominantly relies on manual interpretation by geologists, who meticulously examine seismic attributes including texture patterns, morphological features, and amplitude variations to ascertain fault existence, classification, and structural characteristics (Freeman et al., 2010; Shaw et al., 2005). While this expert-dependent methodology remains fundamental for gas storage development, its labor-intensive nature and time constraints increasingly conflict with the urgent demand for rapid geological characterization in time-sensitive construction projects (Wang et al., 2025). This operational challenge has accelerated the adoption of machine learning (ML) and statistical approaches, particularly through ensemble learning frameworks and feature engineering techniques that systematically optimize seismic attribute combinations to enhance interpretation reliability (Lin et al., 2024). For instance, Di et al. proposed a super-attribute-based classification method integrating Support Vector Machine (SVM) and Multilayer Perceptron (MLP) algorithms with local seismic patterns, demonstrating enhanced fault detection accuracy and computational efficiency in 3D seismic interpretation through its application to polygonal fault systems in New Zealand's Great South Basin (Di et al., 2019). Guitton et al. developed a supervised SVM framework with Gaussian kernels and HOG/SIFT features for 3D seismic fault detection, significantly reducing false positives and demonstrating robustness against mislabeled training data in both synthetic and field datasets (Guitton et al., 2017). Di et al. developed a multi-attribute SVM framework for 3D fault detection, leveraging edge-detection, geometric, and texture attributes to train a classifier. This method successfully detected multi-scale, multi-directional polygonal faults in New Zealand's Great South Basin (Di et al., 2017). Despite advancements in traditional ML-based fault identification, existing methods face limitations in dependency on manual attribute engineering, which restricts adaptability to diverse geological morphologies and multi-scale fault systems. Additionally, challenges persist in computational efficiency for large 3D datasets and robustness against seismic noise or incomplete training labels.

At present, deep learning-based methods excel in complex high-dimensional nonlinear tasks by establishing end-to-end mappings from raw inputs to interpretable geological features, eliminating manual feature engineering through hierarchical representation learning (Zhang et al., 2024b). Their core strength lies in adaptively capturing multi-scale spatial dependencies *via* deep nonlinear transformations, enabling robust fault characterization while maintaining computational tractability for large-scale subsurface analysis (Zhang et al., 2026). For example, Wu et al. pioneered synthetic-data-driven fault segmentation using a class-balanced fully convolutional network, resolving spatial complexity and imbalance challenges to outperform traditional discontinuity attribute methods in both speed and precision (Wu et al., 2019). Zhao et al. developed Fault2SeisGAN, that synthesizes labeled seismic data *via* hybrid loss functions, effectively addressing training data scarcity and improving fault detection model robustness without requiring extensive manual annotation (Zhao et al., 2023). Lin et al. introduced a 2.5D channel attention U-net that integrates multi-slice correlations with lightweight architecture, optimizing fault detection accuracy while minimizing annotation costs (Lin et al., 2022). Li et al. proposes Fault-Seg-Net, an end-to-end deep learning semantic segmentation network that achieves high-precision fault identification in seismic images by integrating multi-scale feature extraction and spatial attention mechanisms (Li et al., 2023a). Tian et al. proposed an integrated “Geology-Geophysics-Data Mining” workflow that enhances identification of strike-slip fault-controlled paleokarst reservoirs through seismic impedance inversion and machine learning, effectively addressing strong heterogeneity challenges in deep carbonate reservoirs (Tian et al., 2023). Further, some researchers (Tang et al., 2023; Wang et al., 2023; Bomfim et al., 2023) have embraced the Transformer framework as an alternative to CNNs for fault recognition. Critically, these methods predominantly focus on statistical correlations in data patterns while neglecting the fundamental causal mechanisms governing fault formation. Specifically: (1) Geophysical mechanism neglect primarily manifested as failure to incorporate first-principles knowledge such as stress-strain relationships controlling rock failure, oversight of geological confounders including rock type variations biasing seismic signals, and ignorance of physical constraints exemplified by friction laws governing brittle-to-ductile transitions. This core deficiency forces models to learn superficial statistical artifacts rather than causal mechanisms. (2) Computer vision dominance compounded by inherited image-centric frameworks that prioritize pixel-level pattern recognition over geophysically meaningful feature learning, thereby treating seismic data as generic images instead of physical field measurements. (3) Grid-induced rigidity where spatial context modeling is constrained by fixed-grid processing pipelines, which intrinsically struggle to resolve subtle fault traces due to inflexible receptive fields. These limitations form a synergistic degradation cycle: Causal blindness necessitates overdependence on visual features, which when processed through grid-based architectures leads to weakened fault sensitivity, ultimately compromising generalization capabilities across geological scenarios.

As a natural extension of deep learning frameworks, graph representation learning (GRL) has gained prominence for its capacity to model associative information through collaborative feature propagation, achieving widespread adoption in industrial and biomedical domains (Zhang et al., 2025a). Typical applications include mechanical fault diagnosis (Yang et al., 2023), equipment health prognostics (Zhang et al., 2024a), disease classification (Sun et al., 2020), and social network analysis (Li et al., 2023b). Within geoscience exploration, GRL has demonstrated preliminary success in tasks such as lithology identification and reservoir characterization. For instance, Geng et al. developed a static-dynamic graph convolutional network enhanced by channel attention mechanisms, which leverages unlabeled data through attention-driven edge information propagation to address label scarcity in lithology interpretation (Geng et al., 2023). Lu et al. further incorporated geological priors into graph-structured logging data, proposing a framework that reduces misidentification rates of natural fractures (NFs) by 12%–18% compared to conventional methods (Lu et al., 2024). These advancements underscore GRL's potential in encoding geological relational priors and handling sparse supervision scenarios. However, the adaptation of GRL to seismic image processing and fault recognition remains notably scarce. Current methodologies predominantly rely on grid-based convolutional operations, failing to exploit graph-structured representations that inherently align with fault networks' topological connectivity and multi-scale spatial dependencies. This gap critically limits the interpretability and physical consistency of fault detection systems when processing seismically complex formations.

Based on the above research background, a multi-knowledge causally embedded graph representation approach for fault identification (FI) in seismic images is proposed. First, utilizing geological prior knowledge, the seismic volume is first discretized into node sets through pixel-to-node transformation. To explicitly capture causal structures, a multi-relational feature computation method integrates: (a) spatial continuity constraints of faults as physical causality priors, and (b) seismic signal characteristics. Guided by these causal priors, Causally chain-graphs (CCGs) are constructed through knowledge-driven edge pruning and reinforcement, with connections constrained by pixel spatial receptive fields to reflect geological causality. These causally structured graphs subsequently undergo feature aggregation *via* graph convolutions, modeling non-Euclidean relationships between nodes. Finally, the new seismic image is converted through the above steps into a series of CCGs, with the fine-tuned model output identifying fault labels. The pixel labeled as faults are connected in the original image to obtain pixel-level seismic faults. The above pipeline evolves from low-level graphs to high-order fault representations, enabling end-to-end pixel-level identification.

The rest of this article is organized as follows. Section 2 introduces the theoretical background about causally geological fault identification from seismic-image. Then, the graph-based geological fault identification method is proposed in Section 3. Effectiveness of the proposed fault identification method is verified on case studies in Section 4. In Section 5, discussions about the influences of prior causally knowledge contained in original seismic images and graph representation learning are given. Finally, the conclusion is given in Section 6.

2. Preliminaries

2.1. Task definition

Faults are geological structures formed by rock fracturing (Tang et al., 2025) and subsequent relative displacement, manifested as discontinuities in seismic reflection events, such as misalignment, distortion, or abrupt amplitude variations (Faleide et al., 2021). Seismic volume fault identification refers to the process of detecting and annotating the spatial distribution, geometric morphology, and kinematic attributes of geological faults within three-dimensional (3D) seismic data volumes. The core objective of this task is to leverage the physical responses of seismic wave propagation (e.g., variations in reflection coefficients, waveform distortions) and integrate geological structural principles to transform implicit fault information embedded in seismic data into quantifiable structural models (Botter et al., 2014).

In Artificial intelligent (AI)-driven geological fault identification method, let the 3D seismic data volume be represented as a tensor $S \in \mathbf{R}^{W\times H\times T}$, and the fault labels as a binary mask $F \in \{0,1\}^{W\times H\times T}$. The objective is to learn a mapping function $f_\theta : S \rightarrow F$, where θ denotes the model parameters. This is achieved by optimizing the objective function:

$$L(\theta) = \sum_i L_{\text{data}}(f_\theta(S_i), F_i) + \lambda L_{\text{physics}} f_\theta(S_i) \tag{1}$$

where L_{data} is a data-driven loss term (e.g., cross-entropy), L_{physics} represents physics-based constraints, such as geometric continuity of faults, consistency of fault displacement. The process of AI-driven geological fault identification is illustrated in Fig. 1.

2.2. Standardization and gain correction method

Due to the geometric spreading characteristics of wave propagation and the intrinsic absorption of reservoirs, seismic waves inevitably undergo amplitude attenuation. This physical phenomenon results in significantly weaker amplitude in deep-layer signals compared to shallow reflections, while energy imbalances across seismic traces further arise from variations in acquisition systems (Choi et al., 2021). To mitigate these challenges, it is imperative to implement data standardization and gain correction as preprocessing techniques. These methods aim to enhance image quality and amplify weak deep reflection signals by compensating for amplitude attenuation and harmonizing energy distribution across seismic traces (Griffiths and King, 2013).

Specifically, data standardization normalizes raw seismic profiles $I_{\text{raw}}(x,t)$ using local statistical measures, with the core formula expressed as,

$$I_{\text{norm}}(x,t) = I_{\text{raw}}(x,t) - \mu(x)\sigma(x) \tag{2}$$

where $\mu(x)$ and $\sigma(x)$ represent the local mean and standard deviation along the time axis t. This process eliminates trace-to-trace baseline shifts and energy disparities, ensuring zero-mean and unit-variance data distributions.

Subsequently, time-varying gain correction compensates for amplitude attenuation through Eq. (3), model the inverse processes of geometric spreading and absorption effect function, thereby enhancing the discernibility of deep weak reflections (Etgen et al., 2009). The processes are shown as follows:

$$C(t) = t^\alpha e^{\beta t} \tag{3}$$

where α represent geometric spreading compensation coefficient, β is absorption attenuation coefficient, which is related to the quality factor Q and dominant frequency f *via* function:

$$\beta = \pi f / Q \tag{4}$$

To further accentuate geological fault interface, the instantaneous amplitude function $A(x,t)$ derived from the Hilbert transform (Johansson, 1999), is employed to extract signal envelopes and reduce phase sensitivity, improving the continuity of discontinuous features, as follows:

$$A(x,t) = \sqrt{I_{\text{gain}}^2(x,t) + H^2\left[I_{\text{gain}}(x,t)\right]} \tag{5}$$

where $I_{\text{gain}}(x,t)$ is amplitude-corrected seismic trace after gain correction, at spatial location x and time t, $H\left[I_{\text{gain}}(x,t)\right]$ represent Hilbert transform of $I_{\text{gain}}(x,t)$.

2.3. The principle of causality

In the interdisciplinary field of computational geophysics and machine learning, causal principles employ formalized Structural Causal Models (SCMs) to delineate the generative mechanisms among variables. Mathematically grounded in structural equations $F : V \times U \rightarrow V$, where V denotes observable variables and U latent variables, this framework transcends traditional statistical correlations. It quantifies causal effects through the do-opera to $P(Y|\text{do}(X=x))$ and disentangles confounders C *via* counterfactual reasoning $P(YX = x|X = x', Y = y')$. Its core strength lies in learning invariant causal representations $\Phi(X)$ that satisfy $P(\Phi(X)|C) = P(\Phi(X))$, thereby maintaining robustness under distributional shifts (e.g., unseen tectonic settings) and providing mathematical guarantees for interpretable decision-making. Further, for the coupled mechanisms of seismic attributes and fault identification, SCMs must explicitly incorporate geophysical priors:

1) Direct causal pathways: geological fault activity F_{Geo} acts as the causal variable, where stress field-induced rock fracturing

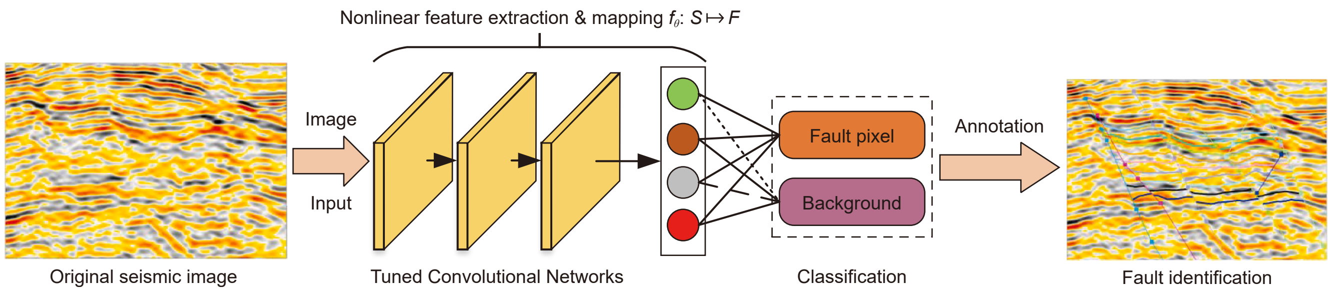

Fig. 1. The process of AI-driven geological fault identification

$\sigma > \sigma_{\text{yield}}$ (where σ is tectonic stress, σ_{yield} denote the rock yield strength) triggers:

- Reduced seismic wave coherence $\left(\Delta\text{Coh} \propto \int |\nabla u - \nabla v| \text{d}t\right)$, where u and v are the wavefield components;
- Curvature anomalies $\kappa = \partial^2 z / \partial x^2 / \left(1 + (\partial z/\partial x)^2\right)^{3/2} > \kappa_{\text{crit}}$, where z denote the horizon depth, κ_{crit} is the curvature threshold;
- Acoustic impedance contrast: $\Delta Z = \rho_1 V_1 - \rho_2 V_2 \Rightarrow |R\uparrow|$, where ρ_1 is the density, V is the wave velocity, R represent the reflection coefficient.

The above processes adhere to the backdoor adjustment criterion $P(F|S) = \sum GP(F|S,G)P(G)$ where S is the seismic attributes, and G denote the geological background.

2) Treat geological context as causal moderators: Geological factors act as causal moderators that systematically alter fault-seismic relationships, two mechanisms require explicit modeling:
   - Tectonic stress regimes control fault geometry: Through Anderson's theory $\theta = f(\sigma_1/\sigma_3)$ (where σ_1 is the maximum principal stress, σ_3 = minimum principal stress), the stress orientation governs fault dip angles θ and extensional regimes create steep normal faults ($\theta \approx 60°$), while compressional regimes generate shallow thrust faults ($\theta < 30°$), altering seismic expression;
   - Sedimentary facies introduce confounding signals: Lithology variations such as channel sands C_{channel} create amplitude anomalies that mimic fault signals $A_{\text{amp}} = g(F,C) + \varepsilon$ (where C is the facies type, and ε represent the random noise), and leading band bodies generate "false fault" reflections, requiring front-door adjustment to isolate true fault effects.

2.4. Graph representation learning

Graph theory aims to transform structured data into associated unstructured graph structure data by mining the internal correlation of objects, and further use graph neural network (GNN) to aggregate learning and evolve the spatial-temporal relationship of graphs.

2.4.1. Graph structure data

Through node embedding and edge connection, the data are transformed into a graph, which can be represent as $G = \{V, E, \mathbf{A}, F\}$ in mathematically. Among them, set V contains all node, and E represent the edge connections. $\mathbf{A} \in \mathbf{R}^{n*n}$ called adjacent matrix, which stores all node relationships. Set F denotes node features, which is the key component of convolution operations. Typical graph constructions are illustrated in Fig. 2.

2.4.2. Graph neural network

As an extension of the Convolutional neural networks (CNN) (Zhang et al., 2024b), Graph convolution aims to aggregate neighbor nodes information, achieving spatial convolution, which can be described as follow,

$$\mathbf{H}_l = \text{f}(\mathbf{H}_{l-1}, \mathbf{A}) \tag{6}$$

where $\mathbf{H}_l$ is the output feature matrix, $\text{f}(\cdot)$ denote convolution function, and $\mathbf{A}$ represent adjacent matrix.

At each layer of the convolution operation, the common mathematical propagation is as follows:

$$\mathbf{H}_l = \sigma\left(\tilde{\mathbf{D}}^{-\frac{1}{2}} \tilde{\mathbf{A}} \tilde{\mathbf{D}}^{-\frac{1}{2}} \mathbf{H}_{l-1} \mathbf{W}_{l-1}\right) \tag{7}$$

where $\mathbf{D}$ is called the degree matrix (Zhang et al., 2019), which is a diagonal matrix with internal elements that conform to $\mathbf{D}_{ii} = \sum_j \mathbf{A}_{ij}$. $\sigma(\cdot)$ denote activate function, and $\mathbf{W}$ is a learning weight matrix.

Introducing the regularized Laplacian matrix $\mathbf{L}$ to a more simplified expression of node relations, the following formula can be defined as

$$\mathbf{L} = \mathbf{U}\boldsymbol{\Lambda}\mathbf{U}^{\text{T}} \tag{8}$$

where $\mathbf{U}$ is a matrix of eigenvectors, and matrix $\boldsymbol{\Lambda}$ contains only eigenvalues. Thus, graph convolution can be written as (Song et al., 2018),

$$\mathbf{H}_l = \mathbf{U} g_\theta(\boldsymbol{\Lambda}) \mathbf{U}^{\text{T}} \mathbf{H}_{l-1} \tag{9}$$

Chebyshev polynomial $g_\theta(\boldsymbol{\Lambda})$ is chosen as the filter with excellent computational efficiency (Wang et al., 2019), which can be defined by

$$g_\theta(\boldsymbol{\Lambda}) \approx \sum_{k=0}^{K-1} \theta_k T_k(\tilde{\boldsymbol{\Lambda}}) \tag{10}$$

where $\tilde{\boldsymbol{\Lambda}}$ is rescaled as $\tilde{\boldsymbol{\Lambda}} = 2\boldsymbol{\Lambda}/\lambda_{\max} - \mathbf{I}_n$, $\lambda_{\max}$ represent the largest element of $\boldsymbol{\Lambda}$, K is the highest order of Chebyshev polynomials, θ_k is

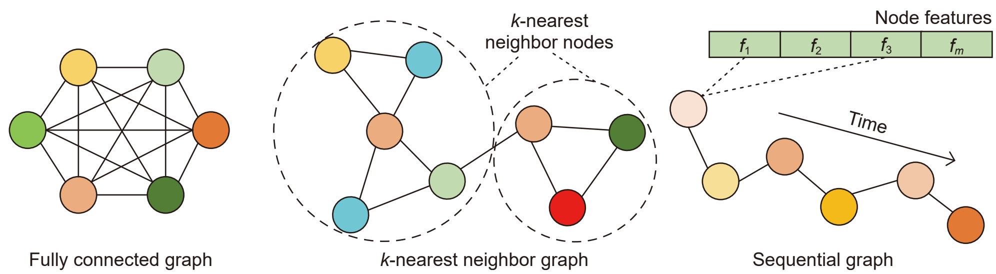

Fig. 2. Typical graphs constructed from different connection method

the Chebyshev coefficient, $T_k(x)$ is the recursive Chebyshev polynomial, defined as

$$\begin{cases} T_0(x) = 1, \\ T_1(x) = x, \\ T_k(x) = 2xT_{k-1}(x) - T_{k-2}(x), (k \geq 2) \end{cases} \tag{11}$$

Finally, the Chebyshev graph convolutional (Cheb_GCN) layer can be defined as (Chen et al., 2020),

$$\mathbf{H}_l = \mathrm{Cheb}(\mathbf{H}_{l-1}, \mathbf{W}) = \sum_{k=0}^{K-1} \theta_k \mathbf{U} T_k(\tilde{\mathbf{\Lambda}}) \boldsymbol{U}^{\mathrm{T}} \mathbf{H}_{l-1} \mathbf{W} \tag{12}$$

where $\mathbf{H}_l \in R^{n*m}$, trainable weight matrix $\mathbf{W} \in R^{m*s}$.

3. Method

3.1. Overview

To spontaneously identify geological faults from monitored seismic volume data for decision-making support in gas storage facility site selection and operation, a graph representation learning-driven method for geological fault identification is proposed in this article. The method relies on the explicit capture and iterative evolution of prior knowledge through graph representation learning, aiming to accurately distinguish fault pixels from geological backgrounds under the constraints of geological mechanism knowledge. Specifically, key steps including: 1) Seismic images preprocessing, 2) Knowledge-enhanced chain-graphs construction, and 3) Geological fault identification. The overall framework of the proposed method is illustrated in Fig. 3.

3.2. Seismic images preprocessing

The preprocessing pipeline operates on raw seismic profiles $I_{\mathrm{raw}}(x,t) \in \mathbf{R}^{P\times P}$ through a cascaded framework designed to decouple interference factors and enhance interpretable features. Initially, data standardization applies local normalization (Eq. (2)) with a sliding window of size $s \times s$, transforming $I_{\mathrm{raw}}(x,t)$ into $I_{\mathrm{norm}}(x,t)$ thereby eliminating spatially varying illumination artifacts and sensor-induced biases to establish amplitude homogeneity across the spatial domain. Subsequently, time-varying gain correction compensates for energy attenuation *via* the decay function $c(t)$ (Eqs. (3) and (4)), generating $I_{\mathrm{corr}}(x,t) \in \mathbf{R}^{P\times P}$ with restored deep-layer signal strength and vertically balanced energy distribution, critical for resolving subtle subsurface structures.

To further suppress phase interference and enhance feature continuity, instantaneous amplitude extraction computes the envelope $A(x,t)$ (Eq. (5)) through Hilbert transform, which removes oscillatory amplitude fluctuations, sharpens fault edges, and reinforces lateral continuity of geological interfaces in $A \in \mathbf{R}^{P\times P}$. Finally, adaptive segmentation divides A into overlapping sub-seismic images (SSIs) of size $M \times M$, controlled by stride S, yielding $\{SSI_k, l\} \in \mathbf{R}^{M\times M}$, enabling multi-scale fault analysis by isolating localized patterns while preserving contextual coherence through controlled overlap. Above hierarchical process systematically addresses illumination inhomogeneity (Eq. (2)), physical attenuation (Eqs. (3) and (4)), phase sensitivity (Eq. (5)), and scale dependency, constructing a standardized representation that bridges mathematical operations to geological interpretability.

3.3. Knowledge of causally chain-graphs construction

Building upon preprocessed seismic volume images, the core contribution of this study lies in transforming a series of preprocessed Sub-Seismic Images (SSIs) into corresponding Causally chain-graphs through causality-driven multi-knowledge embedding and fused relational capturing, thereby providing geologically causal learnable representations for intelligent fault recognition. The process of knowledge Causally chain-graphs construction is illustrated in Fig. 4.

3.3.1. Multi-knowledge causality embedding

Aim to convert 2D seismic image $SSI_k \in \mathbf{R}^{M\times M}$ to a causally structured $CCG = \{V, F, E, A\}$, each pixel in *SSI* is uniquely mapped to a node in *CG*, where the coordinates (i,j) in *SSI* is defined as a node $v_{i,j} \in V$, resulting in $N = M^2$ nodes. To explicitly encode geological causal priors (physical mechanisms & confounders), the most important geographic prior knowledge screened by experts is used to calculate the fault characteristics of nodes, including directional gradient constraint vector $G_\theta(x,y,t)$ (which is embedding fault spatial continuity as physical causality prior), amplitude anomaly detection vector $A(x,y)$, and coherency cube constraint vector $C(x,y)$. The formulas are defined as follows:

$$G_\theta(x,y,t) = \omega_\theta * \frac{\partial}{\partial t}[\nabla_\theta I(x,y,t)] \tag{13}$$

where (x,y,t) is spatial coordinates in the *SSI*, with (x, y) denote lateral positions and t represents time or depth, θ represent direction of gradient computation (e.g., horizontal, vertical, or diagonal), $\nabla\theta$ denote directional gradient operator along θ, quantifying local intensity variations, $\frac{\partial}{\partial t}$ is the partial derivative along the time/depth axis, enhancing discontinuities in seismic reflections, ω_θ is the directional weighting function to suppress noise in non-fault orientations, and * represent convolution operator for smoothing gradient responses. This formula highlights abrupt changes at fault boundaries by combining multi-directional gradients while attenuating smooth variations in continuous seismic horizons.

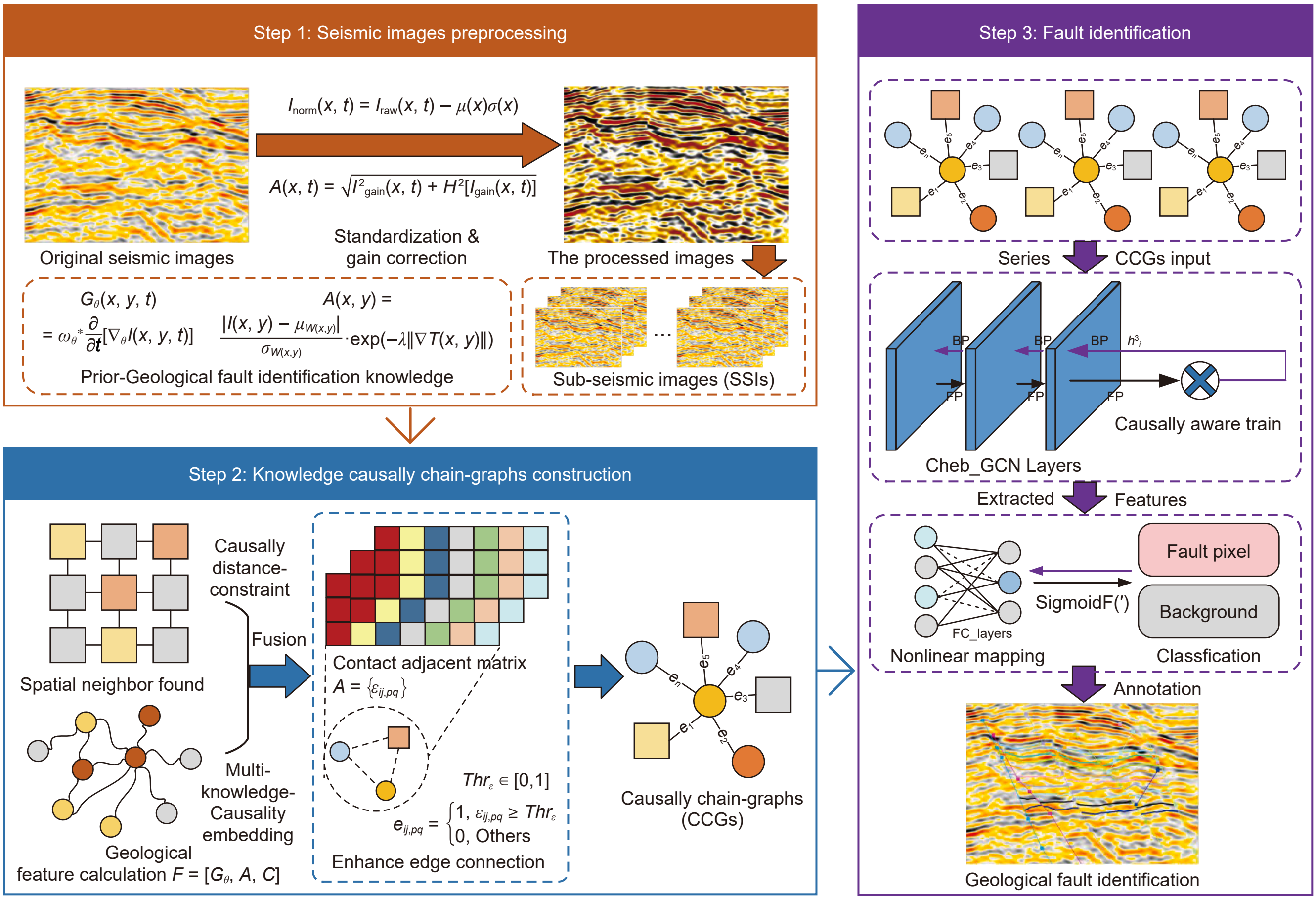

Fig. 3. The framework of the proposed geological fault identification method

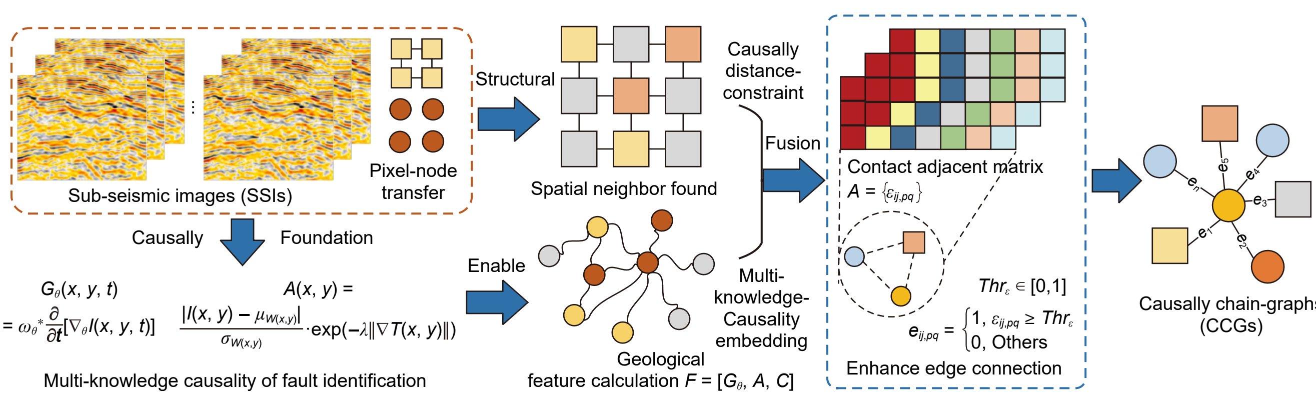

Fig. 4. The process of knowledge causally chain-graphs construction

$$A(x,y) = \frac{\left|I(x,y) - \mu_{W(x,y)}\right|}{\sigma_{W(x,y)}} \cdot \exp(-\lambda\|\nabla T(x,y)\|) \tag{14}$$

where $I(x,y)$ represent amplitude value at position $(x,\ y)$ in the seismic volume, $\mu_{W(x,y)}$ is the mean amplitude within a sliding window W centered at (x,y), $\sigma_{W(x,y)}$ denote the standard deviation of amplitudes within W, $\nabla T(x,y)$ is the gradient of instantaneous phase, reflecting phase discontinuities, and λ represent the attenuation coefficient controlling the suppression of phase-related noise. This metric quantifies the likelihood of a pixel belonging to a fault by evaluating local amplitude deviations and phase incoherence.

$$C(x,y) = 1 - \frac{\sum_{k=1}^{K} \geq \left\| u_k - \widehat{u} \right\|^2}{(K-1)\left\| \widehat{u} \right\|^2} \tag{15}$$

where u_k denote the waveform vector of the k-th adjacent seismic trace within the neighborhood $\widehat{u}$ is the mean waveform vector of K neighboring traces, K represent the number of traces in the local neighborhood (e.g., 3×3 or 5×5), and $\|\cdot\|$ is the Euclidean norm of the vector. Coherency measures waveform similarity among adjacent traces, with low coherency ($C \approx 0$) indicating fault-induced discontinuities.

By traversing all the nodes $v_{i,j} \in V$ in the input *SSI* and calculating these causally relevant fault representations, each node $v_{i,j}$ is assigned a third-order node feature $f_{i,j} \in \mathbf{R}^3$, formulated as:

$$f_{i,j} = [G_\theta(i,j), A(i,j), C(i,j)] \tag{16}$$

3.3.2. Fused relational capturing

As the embedded node features encode seismic texture, amplitude anomalies, and structural continuity, edges $e_{ij,pq} \in E$ are established between nodes $v_{i,j}$ and $v_{p,q}$ under causality-guided fused relational capturing. Guided by the principle of geological continuity (a core causal prior), the spatial connection of nodes is limited to the fifth-order neighboring nodes to enforce localized geological causality, and the Euclidean distance formula is used to strengthen causal dependencies between potentially related fault structures.

$$\sqrt{(i-p)^2 + (j-q)^2} \leq d_{\max} \tag{17}$$

Furthermore, in the filtered Euclidean neighbor space, the correlation edge weight $\varepsilon_{ij,pq} \in A$ between the nodes are calculated using a Gaussian kernel to quantify causal relationships under geological constraints:

$$\varepsilon_{ij,pq} = \exp\left(- \frac{\left\| f_{ij} - f_{pq} \right\|^2}{\sigma} \right) I_{\text{neighber}}\left(v_{ij}, v_{pq}\right) I_{\text{distance}}\left(v_{ij}, v_{pq}\right) \tag{18}$$

where I_{neighber} and I_{distance} enforce spatial and feature-based causal constraints. Further, to explicitly encode geological causality and suppress spurious correlations, threshold parameter $Thr_\varepsilon \in [0,1]$ is used to remove those weak node connections lacking causal evidence:

$$e_{ij,pq} = \begin{cases} 1, \varepsilon_{ij,pq} \geq Thr_\varepsilon \\ 0, \text{others} \end{cases} \tag{19}$$

Among them, $e_{ij,pq} = 1$ denote that causally significant edges are preserved, while represent spurious connections to be removed. Then, the adjacency matrix $A \in \mathbf{R}^{N\times N}$ is constructed as a sparse representation of these causally validated weighted connections. The final CCG preserves causally relevant seismic features while reducing computational overhead through localized connectivity, maintaining geological causal topology for efficient analysis using graph-based algorithms.

3.4. Geological fault identification

To effectively model geological causal dependencies for high-precision fault identification in seismic volumes, a graph learning model that hierarchically integrates multi-scale causal patterns is constructed. This framework addresses limitations of pixel-based methods by explicitly encoding causal relationships and geological attributes within causally chain-graphs.

(a) Graph learning model construction

The model leverages a three-layer Chebyshev Graph Convolutional Network (ChebGCN) to iteratively propagate and refine node features along causally constrained connection, followed by fully connected layers to map aggregated causal graph representations to geological fault probabilities. Each ChebGCN layer processes the input graph $CCG = (A, F)$, where $F \in \mathbf{R}^{N\times 3}$ contains node features and $A \in \mathbf{R}^{N\times N}$ is the causally validated sparse adjacency matrix. Leveraging the spectral convolution defined in Section 2.3, the l-th layer updates node embeddings to encode causal relationships:

$$\mathbf{H}_l = \text{LeakyReLU}\left(\sum_{k=0}^{K-1} \theta_k \mathrm{U} T_k(\tilde{\mathbf{\Lambda}}) \mathbf{U}^{\mathrm{T}} \mathbf{H}_{l-1} \mathbf{W} \right) \tag{20}$$

where $H(0) = F$, $K = 3$ and LeakyReLU ($\alpha = 0.01$) mitigates gradient vanishing. The three ChebGCN layers progressively refine causal node representations from $\mathbf{R}^{N\times 3}$ to $\mathbf{R}^{N\times 64}$, $\mathbf{R}^{N\times 32}$, and $\mathbf{R}^{N\times 16}$, respectively. Global graph features are then extracted *via* mean pooling and fed into two FC layers (dimensions 16 → 8→2) with dropout $p = 0.5$, producing fault probabilities $\widehat{y} \in \mathbf{R}^{N\times 2}$. The model is trained end-to-end using weighted cross-entropy loss to account for geological class imbalance:

$$L = -\sum_{i=1}^{N} [\beta y_i \log \widehat{y}_i + (1-\beta)(1-y_i)\log(1-\widehat{y}_i)] \tag{21}$$

where $\beta = 0.8$ counteracts class imbalance between fault $y_i = 1$ and non-fault $y_i = 0$ nodes based on geological prevalence.

(b) Geological fault identification

Following the aforementioned preparations, the Causally chain-graphs and causally aware graph learning model required for the fault identification task have been fully prepared. The complete workflow is thus outlined as follows:

Step 1: Supervised training: labeled fault traces in SSI are converted to node-level labels in CCGs using coordinate mapping. The ChebGCN model is optimized on 70% training data with Adam (η = 10–3), validated on 10% data for early stopping to preserve causal generalization.
Step 2: Graph structural adaptation: For new seismic data, the SSI-to-CG conversion (Section 3.1) is applied to generate input graphs with preserved causal topology, preserving geological topology through edge constraints I_{neighbor} and I_{distance}.
Step 3: Generalization testing: The trained model predicts fault probabilities for all nodes in unseen CCGs. Post-processing with non-maximum suppression (NMS) removes spurious correlations, and node classifications are projected back to original SSI coordinates, enabling pixel-accurate causal fault localization.

4. Case study

4.1. Preparations

In order to verify the effectiveness of the proposed method, a gas storage construction and operation formation in central China was used as the research object to test the model ability of geological fault identification. The selected site for gas storage

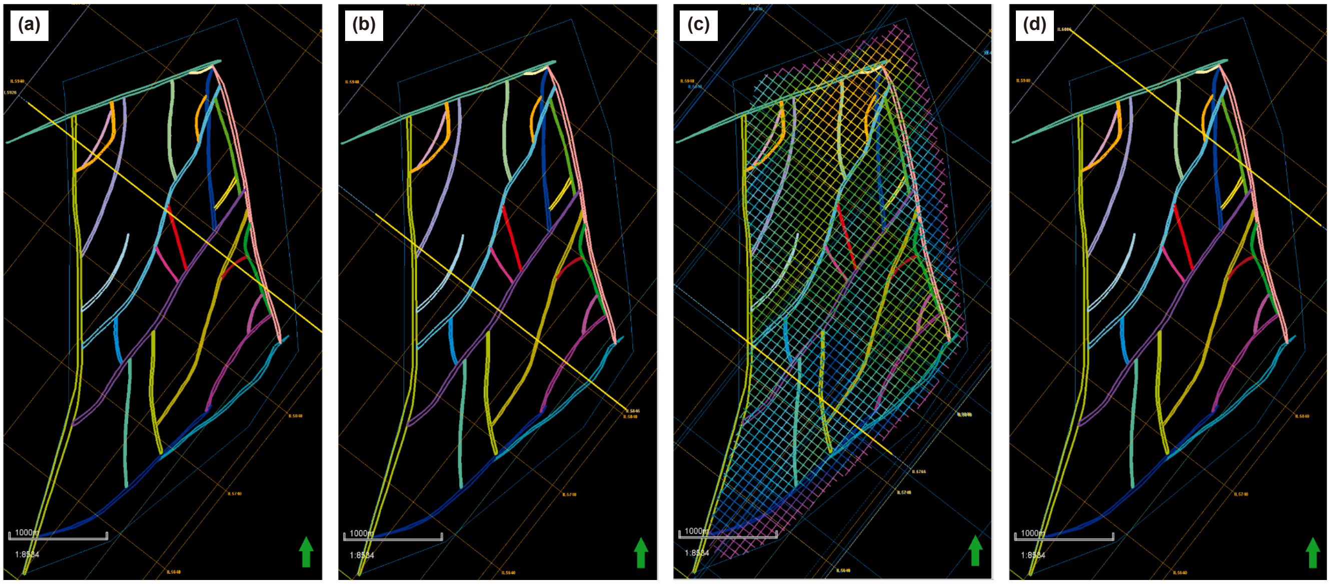

Fig. 5. Position of the seismic profile of each main survey line: **(a)** Southwest profile line, **(b)** central south profile line, **(c)** north-central profile line, **(d)** northeast profile line

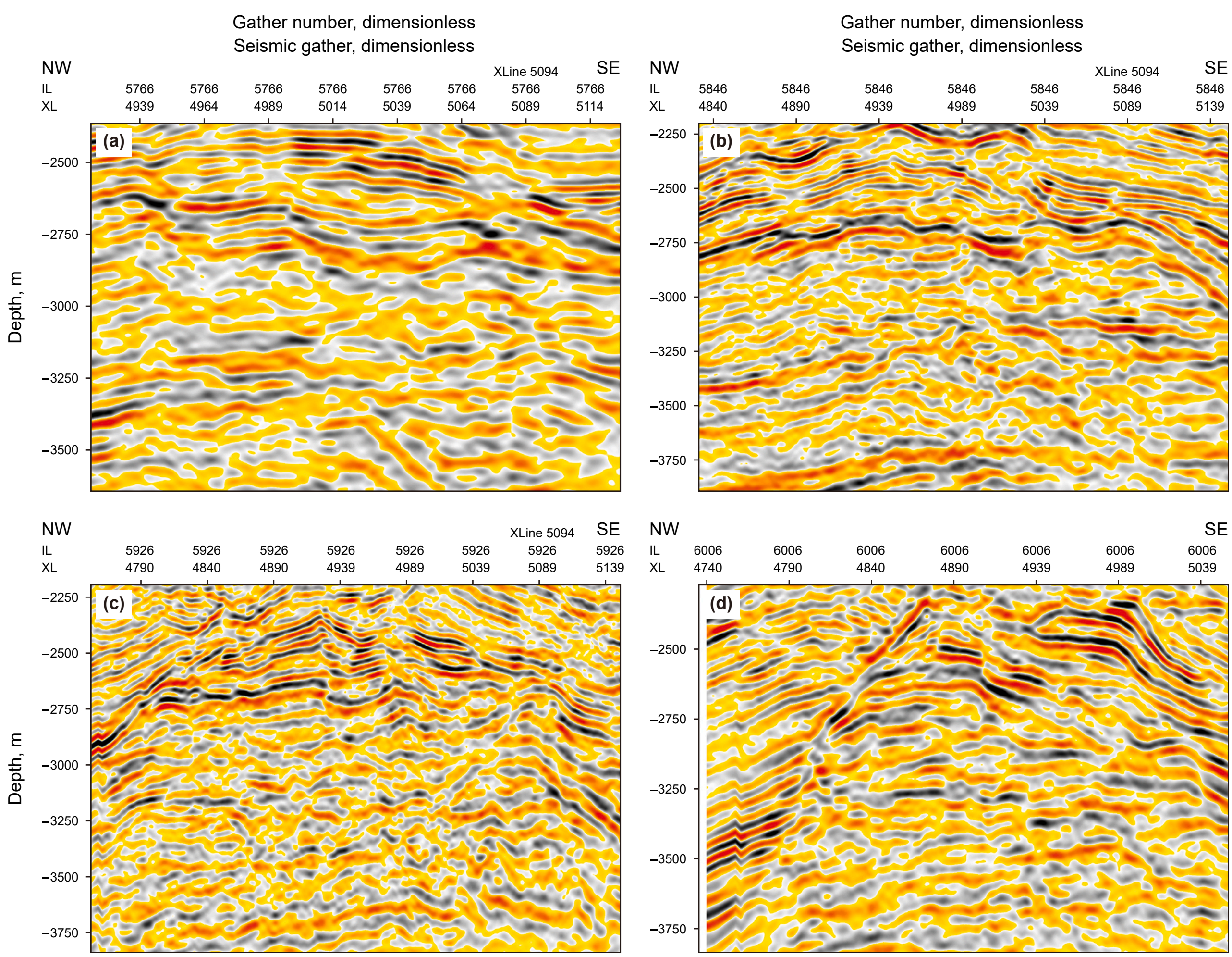

Fig. 6. Segmented profile seismic images of main survey line: **(a)** Southwest profile line, **(b)** central south profile line, **(c)** north-central profile line, **(d)** northeast profile line

construction is situated at the structural high of the northern Central Uplift Belt in a depression, characterized by a complex anticlinal structure formed over bedrock uplift. The block exhibits burial depths ranging from 2700 to 3154 m, with its two-dimensional cross-sectional view presenting a wedge-shaped quadrilateral geometry. The shape of the plot and the position of each main survey line are shown in Fig. 5, while the segmented profile seismic images are shown in Fig. 6.

This study employs 2D seismic profiles for geological fault identification and interpretation. The original data were obtained from continuous profiles starting at trace number 5486 (bottom survey line) to trace number 6238 (top survey line), sampled at 8-trace intervals to yield 94 valid seismic profiles. All 2D images were randomly shuffled, with 70 samples allocated to the training set and the remaining 24 used for testing. To enhance the training samples, 230 synthetic seismic profile images were generated using a Generative against neural (GAN) model. These synthetic images, combined with the 70 original samples, formed a training set of 300 images, which were manually annotated for supervised training. Similarly, a test set containing 50 seismic profile images (comprising a mix of augmented synthetic and original data) was utilized to evaluate model performance. The details of the proposed graph learning model are listed in Table 1.

4.2. Result analysis

The original 2D seismic volume profile with dimensions of 1600 $\times$ 1200 was divided into 40 sub-images using a sliding window of size 40 $\times$ 30. These sub-images were subsequently converted into 40 Causally chain-graphs for binary classification-based fault recognition. To evaluate the performance of the proposed method, average results from ten experiments were statistically analyzed. Specifically, the classification confusion matrices for 9 key profiles in F1-score were presented in Fig. 7, while the fault recognition results along the main survey line were illustrated in Fig. 8.

The experimental results demonstrate the superior performance of the proposed graph representation learning framework in addressing pixel-level fault identification within complex geological settings. In the tested anticlinal structure of Central China's gas storage formation (burial depth: 2700–3154 m), the model achieved a mean accuracy of 93.11% (range: 88.91%–95.99%) and an F1-score of 0.758 across ten trials, as evidenced by the normalized confusion matrices in Fig. 7. This performance gain stems from three synergistic innovations: First, the topology-aware chain graph construction explicitly encodes fault networks' non-Euclidean spatial dependencies through pruned edge connections, effectively mitigating seismic noise interference in deep wedge-shaped formations (Figs. 5 and 6). Second, the geologically constrained node features, integrating spatial continuity priors and multi-scale signal characteristics, enable ChebGCN layers to propagate fault features adaptively across non-grid neighborhoods—critical for detecting subtle faults (<5% amplitude variations) in bedrock uplift zones. Third, the end-to-end mapping from raw seismic volumes (Fig. 8) to pixel-wise classifications eliminates handcrafted feature engineering biases, allowing the model to preserve fault topology integrity while handling irregular seismic textures in anticlinal cores. The minimum F1-score (0.63) observed in Profile #5 correlates with its ambiguous fault-karst coupling signatures, whereas the maximum F1 (0.84) in Profile #7 reflects enhanced discriminability for isolated faults through high-order graph convolutions. These quantitative outcomes, combined with the main survey line visualization (Fig. 8), confirm the framework's capability to balance detection sensitivity (minor fault recovery) and operational robustness (false alarm suppression), providing reliable geological constraints for gas storage integrity management.

Table 1
The details of the proposed graph learning model

Components	Input shape	Output shape	Activate $f(\cdot)$	Param K	Loss $L(\cdot)$
ChebGCN_1	1200*3	1200*100	LeakyReLU $(\cdot)$	4	CE_loss
ChebGCN_2	1200*100	1200*300		4	
ChebGCN_3	1200*300	1200*200		4	
FC_Layer_1	1200*100	1200*50		/	
FC_Layer_2	1200*50	1200*2	Sigmoid $(\cdot)$	/	

Based on the identified geological fault, the W23 gas storage facility, situated in the northern Central Uplift Belt of the Dongpu Depression, is governed by a NE-SW-oriented fault system (30–50 m throws) categorized into regional (Class II), block-bounding (Class III), and minor intra-block (Class IV/V) faults. Structural patterns are dominated by step-type and Y-shaped faults, with northeastward narrowing trends suggesting favorable reservoir-seal configurations. The block features late-stage reactivation of basement faults, limited syn-sedimentary activity, and gentler dips (45°–60°) along marginal controlling faults. Furthermore, in the construction and operation of gas storage facilities, the NE-SW trending fault system in the W23 block presents critical engineering risks: late-stage tectonic reactivation and brittle deformation may trigger fault activation under cyclic injection-production stresses, requiring operational optimization to mitigate perturbations; gently dipping boundary faults and NE-trending structural narrowing could compromise caprock integrity, necessitating dynamic seal assessments; interactions between Y-shaped/step-type main faults and secondary faults exacerbate reservoir permeability anisotropy, demanding 3D geological modeling for well placement optimization; X-shaped fault intersections and abrupt trend changes may induce stress concentration, recommending micro-seismic monitoring and leakage early-warning systems. A risk management framework integrating multi-scale fault characterization and dynamic geomechanical responses is essential to ensure safe and efficient operations. Further, the causality-aware framework is not limited to gas storage sites but is readily transferable to fault identification in various hydrocarbon reservoirs, owing to its foundation in universal geological principles.

4.3. Comparative experiments

To further validate the performance of the proposed method, comparative experiments were conducted against both traditional machine learning (ML) and advanced deep learning (DL) models. The evaluated models include Support Vector Machine (SVM), Random Forest (RF), K-means Clustering (K-means), Adaptive Boosting (AdaBoost), U-Net Convolutional Neural Network (U-Net), Convolutional Neural Network (CNN), Vision Transformer (ViT), and the proposed Graph learning model (ChebGCN model). All experiments utilized the same training-testing data splits described in Section 4.2. Configuration details for each model are provided in Table 2, while critical training metrics are summarized in Table 3. To ensure statistical robustness, each model was independently trained and tested ten times under identical conditions, with Mean Accuracy Error (MAE) and Root Mean Square Error (RMSE) results aggregated and visualized in Fig. 9 (See Table 3).

The proposed ChebGCN model achieves state-of-the-art performance in geological fault identification, surpassing both traditional machine learning and deep learning baselines in accuracy and efficiency. Quantitative evaluations demonstrate that ChebGCN attains the lowest 5.61% MAE and 7.05% RMSE, outperforming traditional ML

Table 2
Details of comparative model settings

Model	Key parameters
SVM	Kernel: RBF; C: 1.0; Gamma: 0.01; Tolerance: 1e-3
RF	N_estimators: 200; Max_depth: 15; Min_samples_split: 5; Criterion: Gini
K-means	N_clusters: 10; Max_iter: 300; Init: k-means++; Tolerance: 1e-4
AdaBoost	Base estimator: Decision Tree (max_depth = 3); N_estimators: 100; Learning rate: 0.1
U-Net	Encoder: 4 blocks (Conv2D 3 → 64→128 → 256→512); Decoder: 4 blocks (UpConv + skip connections); Dropout: 0.2
CNN	3 layers: Conv2D (3 → 16→32 → 64, kernel = 3×3); Pooling: MaxPool (2×2); FC: 64 → 10
ViT	Patch size: 16×16; Layers: 12; Heads: 12; Hidden dim: 768; MLP dim: 3072; Dropout: 0.1
ChebGCN	3 layers: ChebConv (input→100 → 300→200); $K = 4$ (polynomial order); Normalization: BatchNorm; Dropout: 0.3

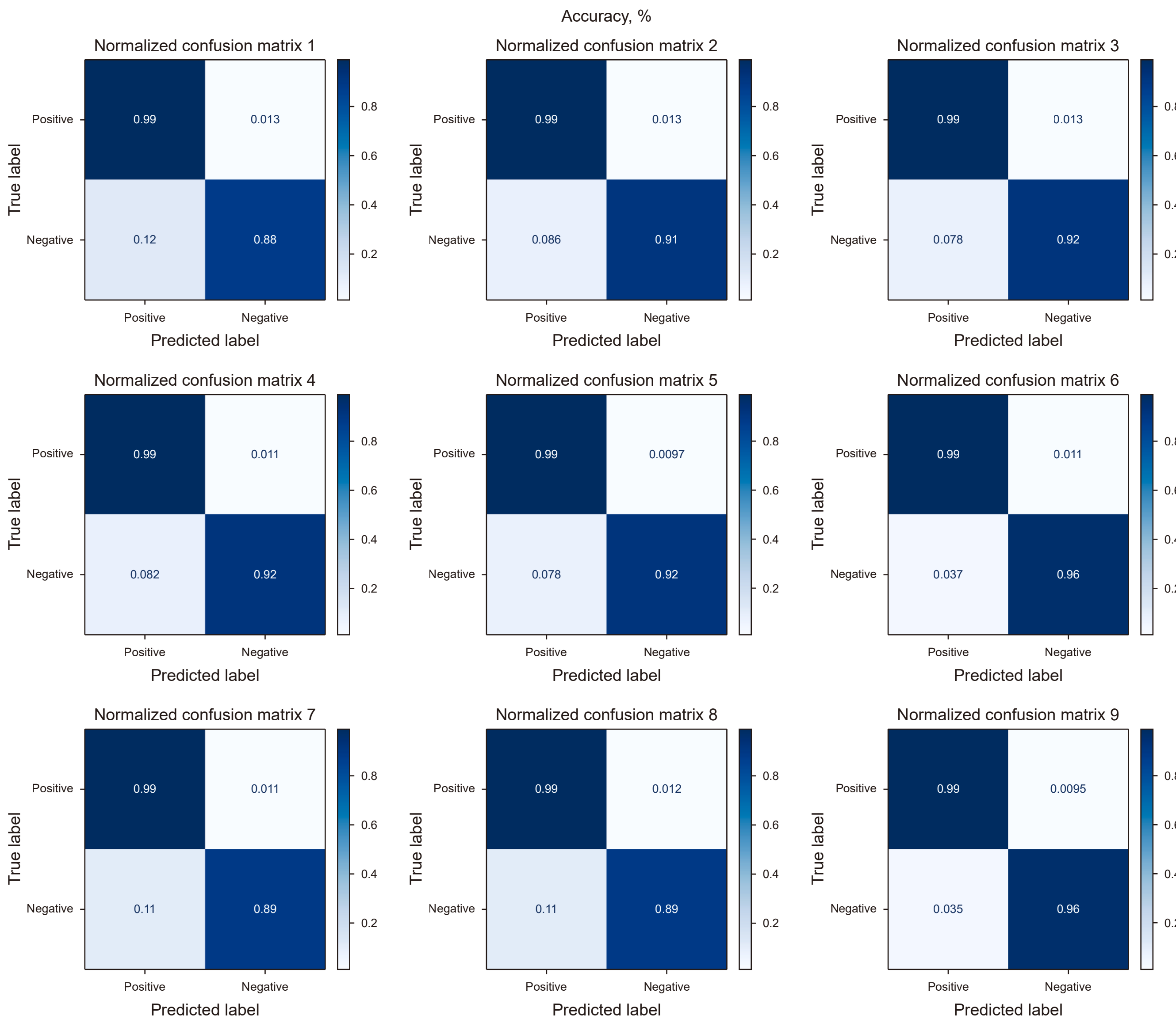

Fig. 7. Classification results in 9 crucial segmented profile seismic images

methods (MAE: 17.67%–26.05%; RMSE: 22.44%–29.99%) and advanced DL models such as U-Net and Vision Transformer (ViT). Specifically, U-Net yields MAE and RMSE values of 7.82% and 10.45%, while ViT exhibits higher errors with 8.95% MAE and 12.05% RMSE, indicating limitations in capturing fault networks' topological dependencies. This performance gap, quantified by MAE and RMSE differences of 1.69%–3.61% and 2.48%–4.00% between ChebGCN and DL models, underscores the superiority of graph-structured learning. ChebGCN's topology-aware architecture explicitly encodes geological spatial continuity through pruned edge connections and non-Euclidean neighborhood aggregation, whereas U-Net's grid-based convolutions and ViT's global attention mechanisms struggle to model multi-scale fault relationships and sparse spatial dependencies inherent to seismic data.

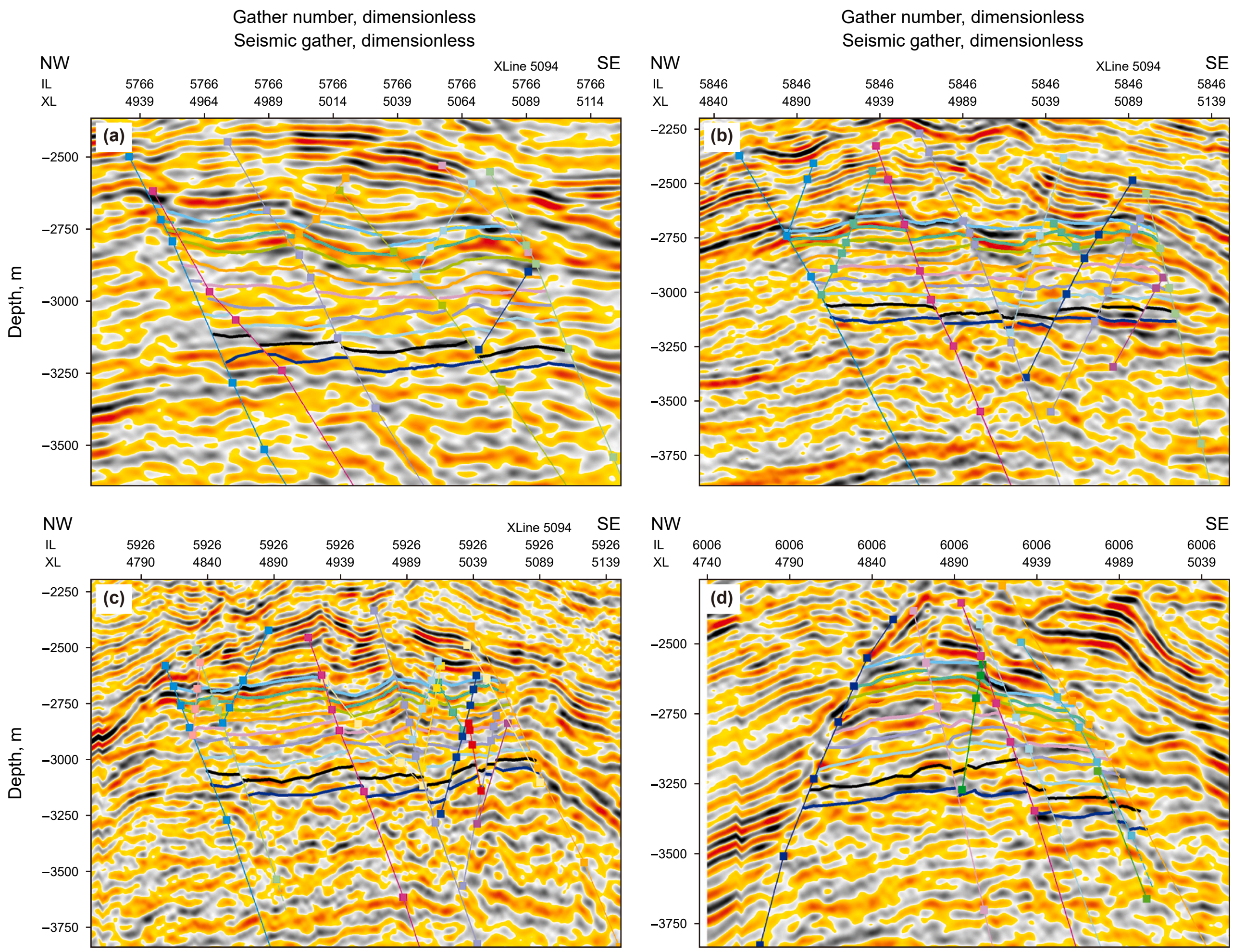

Fig. 8. Fault interpretations in sequence profile seismic images of main survey line: **(a)** Southwest profile line, **(b)** central south profile line, **(c)** north-central profile line, **(d)** northeast profile line

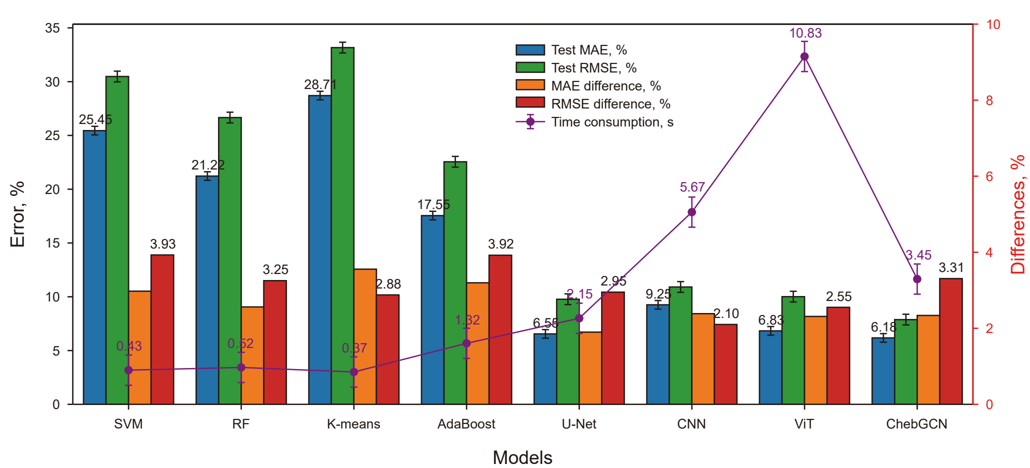

Fig. 9. Comparative results in onsite seismic image tests

ChebGCN further balances computational efficiency with high accuracy, addressing a critical limitation of existing approaches. While traditional ML methods exhibit fast inference times (0.37–0.52 s), their high error rates render them unsuitable for precise fault detection. Conversely, DL models like ViT and CNN incur substantial computational costs (10.83 and 5.67 s, respectively), hindering practical deployment. ChebGCN achieves a competitive inference time of 3.45 seconds—3.1× faster than ViT and 1.6× faster than CNN—while maintaining superior accuracy. This efficiency arises from its sparse graph representation, which

Table 3
Key indexes of comparative models training processes

No.	Models	The number of trainable parameters	Error, %		Times, s
			MAE	RMSE	
1	SVM	3, 418	22.47	26.55	2.01
2	RF	46, 875	18.66	23.41	8.46
3	K-means	-	25.15	30.29	0.6
4	AdaBoost	8, 742	14.35	18.63	7.28
5	U-Net	78, 549, 483	4.65	6.82	11.73
6	CNN	3, 627, 954	6.87	8.81	2.45
7	ViT	125, 486, 552	4.52	7.46	18.76
8	ChebGCN	5, 943, 758	3.84	4.57	5.58

minimizes redundant computations by leveraging geologically constrained edge connections. Combined with GAN-augmented training data, the framework achieves 93.11% identification accuracy on real-world seismic profiles, demonstrating its robustness in complex anticlinal structures and practicality for gas storage infrastructure planning.

To mitigate the potential risk of overfitting associated with a single dataset and to further validate the generalizability of the proposed method, a classic public dataset II for fault identification in seismic volumes was utilized to evaluate the performance of our approach (Wu et al., 2019). This dataset comprises a total of 200 seismic section images, which were randomly split into training and test sets in a 7:3 ratio. Furthermore, for comparative experiments, established models including the U-Net model used with the aforementioned public dataset and a classical CNN model were employed. The learning rate for all models was uniformly set to 0.01. Each model was independently tested 10 times, and the results with error bars are plotted in Fig. 10.

Based on the comparative results on the public benchmark dataset, the proposed ChebGCN model demonstrates superior performance, achieving the lowest RMSE on both the training set (4.05) and, more importantly, the test set (4.88). This consistent outperformance over the established U-NET (test RMSE: 6.29) and CNN (test RMSE: 7.75) models validates its enhanced generalization capability for fault identification across different geological contexts. The key to this robust performance lies in our method's core innovation: the causally embedded graph structure. Unlike the U-NET and CNN, which operate on local pixel neighborhoods and can be misled by seismic noise, our graph model explicitly encodes geological prior knowledge. The multi-knowledge constraints—spatial continuity, amplitude anomaly, and coherency—collectively guide the model to distinguish genuine fault signals from spurious noise. This is precisely why our RMSE is significantly lower; the model is not merely fitting data patterns but is structurally constrained to seek geologically plausible solutions. The smaller gap between our model's training and test RMSE, coupled with the lower error bars, further attests to its stability and reduced overfitting. Furthermore, as this public dataset is a synthetic seismic volume with inherent noise, all models achieve a lower absolute RMSE compared to their performance on our real-world field dataset. This is expected, as synthetic data typically presents a cleaner, more structured learning environment. Nevertheless, even in this setting, the significant performance margin of our method underscores that its ability to leverage geological causality provides a fundamental advantage, enabling it to generalize effectively to unseen seismic data while maintaining resilience to noise.

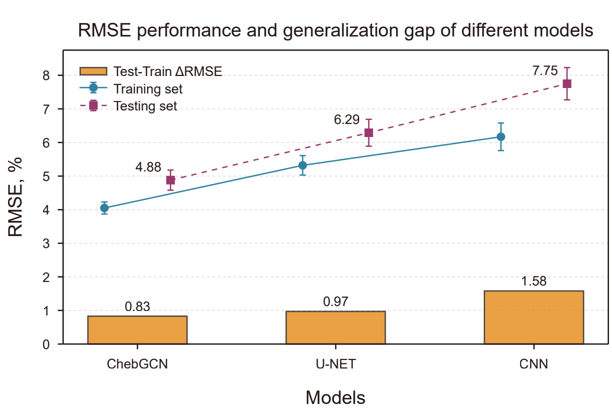

Fig. 10. Additional comparative experiments in dataset II

5. Discussions

5.1. Ablation studies of knowledge embedding

To quantitatively evaluate the contribution of each proposed knowledge-embedding module, a comprehensive ablation study was designed and conducted. The objective is to isolate and measure the performance impact of individual components by systematically removing them from the full model. All experiments were performed on the same dataset and partition described in Section 4.1. To ensure statistical robustness, each model configuration was trained and evaluated over 10 independent runs with random initializations, and the average performance metrics are reported for comparison. The following seven model variants are compared:

Full model (proposed): The complete framework integrating all five knowledge modules: Multi-knowledge Causality Feature Embedding, Geological Continuity-driven Local Connectivity, Euclidean Distance-based Reinforcement, Feature Similarity-based Quantification, and Causally Significant Edge Pruning.

Ablation 1 (without Multi-knowledge Features): This variant removes the Multi-knowledge Causality Feature Embedding, replacing the expert-designed feature vector v_i with simple, raw seismic amplitude values at the node location.

Ablation 2 (without local connectivity): This variant abandons the Geological Continuity-driven Local Connectivity constraint by constructing a fully-connected graph within each seismic image patch instead of using the fifth-order neighborhood.

Ablation 3 (without Euclidean distance): This variant eliminates the Euclidean Distance-based Reinforcement of causal dependencies, setting all edge weights based solely on feature similarity without considering spatial distance.

Ablation 4 (without feature similarity): This variant removes the Feature Similarity-based Quantification using the Gaussian

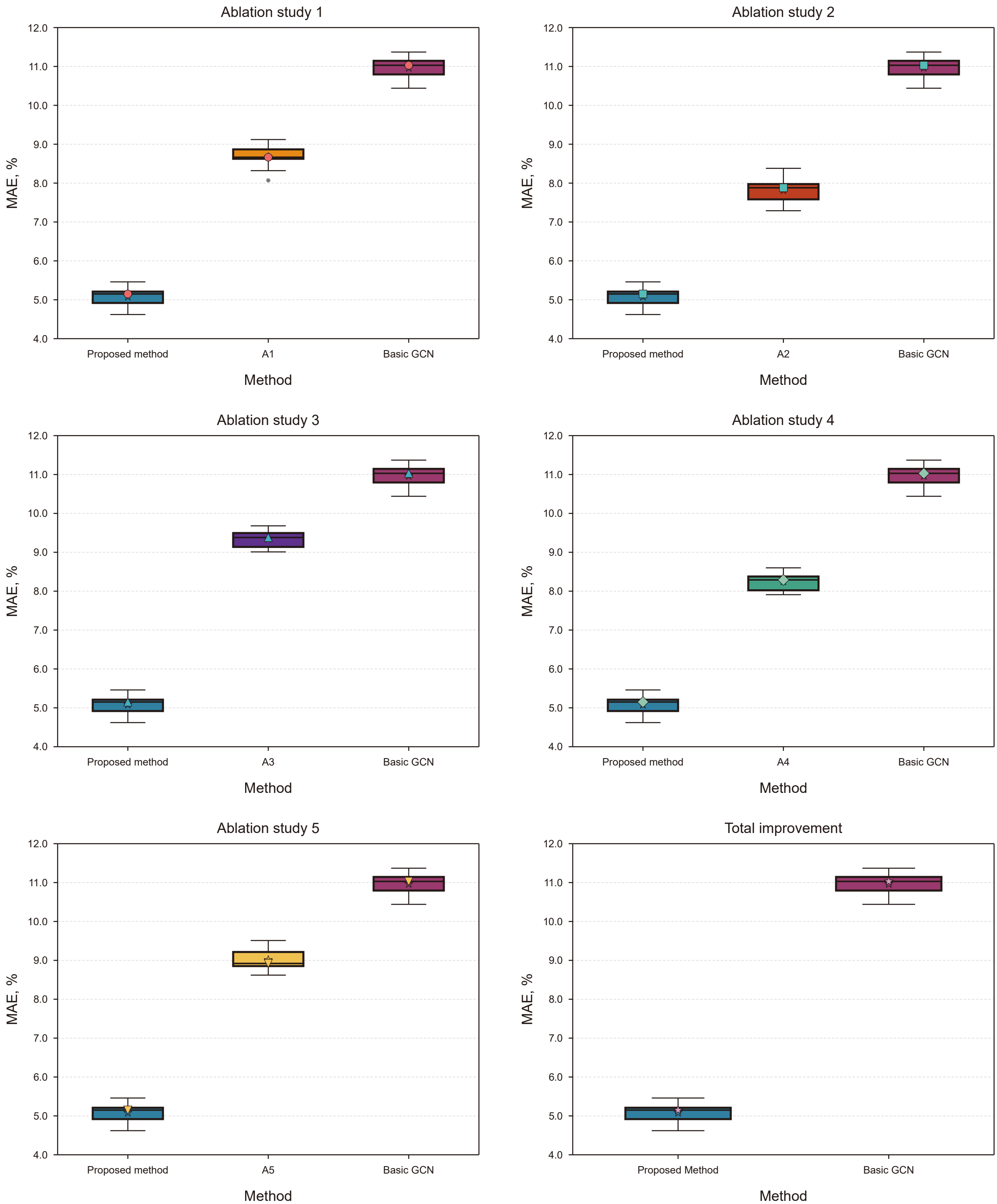

Fig. 11. Ablation experiences of knowledge capture module

kernel, relying exclusively on Euclidean distance within the local neighborhood to calculate edge weights.

Ablation 5 (without edge pruning): This variant disables the Causally Significant Edge Pruning by setting the threshold τ_c to zero, retaining all potential connections within the local neighborhood regardless of their causal strength.

Baseline (basic GCN): This model replaces the entire causally embedded graph construction with a simple graph built using K-

Nearest Neighbors (K-NN) in the pixel space and uses a standard GCN for inference, representing a baseline without any explicit geological knowledge.

The results of each ablation experiment, using MAE as the evaluation metric, are presented in box plots in Fig. 11, as follows:

Based on the comprehensive ablation study results, the proposed method demonstrates decisive and consistent superiority, achieving a remarkably low mean MAE of 5.08%—significantly outperforming the Basic GCN baseline (MAE: 10.96%) by a substantial margin of 5.88 percentage points. This performance gap unequivocally validates the fundamental advantage of embedding geological causal priors into the graph representation learning framework. The systematic performance degradation across the ablation studies provides clear insights into the contribution of each knowledge module:

(1) The most severe performance drop was observed in Ablation 3 (without Euclidean Distance), which yielded the highest MAE (9.34%) among all ablated versions. This establishes that reinforcing causal dependencies based on spatial proximity constitutes the single most critical component for accurate fault identification.
(2) Ablation 1 (without Multi-knowledge Features) also caused a major performance decline (MAE: 8.67%), confirming that replacing the expert-designed causal feature vector with raw seismic amplitudes severely impairs the model's ability to discern subtle fault patterns.
(3) The significant performance deterioration in Ablation 5 (without Edge Pruning, MAE: 9.01%) highlights the crucial importance of removing spurious connections through causal validation, as retaining all potential edges introduces substantial noise that compromises identification accuracy.

Furthermore, the proposed method exhibits the lowest standard deviation (0.2357%) across all 10 independent runs, demonstrating superior robustness and stability—an essential characteristic for practical applications in gas storage safety. The hierarchical performance decline from the full model through the ablations to the baseline provides compelling evidence that the synergistic integration of all knowledge modules is paramount for achieving high-precision, noise-immune fault identification.

5.2. Influence of geological knowledge causality

The proposed multi-knowledge embedding graph representation-driven geological fault identification (FI) method relies on prior knowledge embedding approaches and constraint ranges. Section 3.3 elaborates on the methodology of integrating structural knowledge-enhanced causally chain graphs through structural spatial distance-constraint and prior geological knowledge-embedding techniques. To ensure optimized model performance, comparative experiments were conducted to investigate parameter selection and detailed settings for knowledge-related components. This systematic analysis aims to provide empirical guidelines for balancing geological prior integration with data-driven learning in complex fault system characterization.

5.2.1. Causally distance constraint

To investigate fault continuity exploration in structured 2D seismic volume images while balancing computational efficiency and signal-to-noise ratio (SNR), a series of experiments were designed to evaluate spatial distance constraints. Specifically, five distance metrics: Chebyshev distance (ChebD), Euclidean distance (EucD), Cosine distance (CosD), Mahalanobis distance (MahD), and

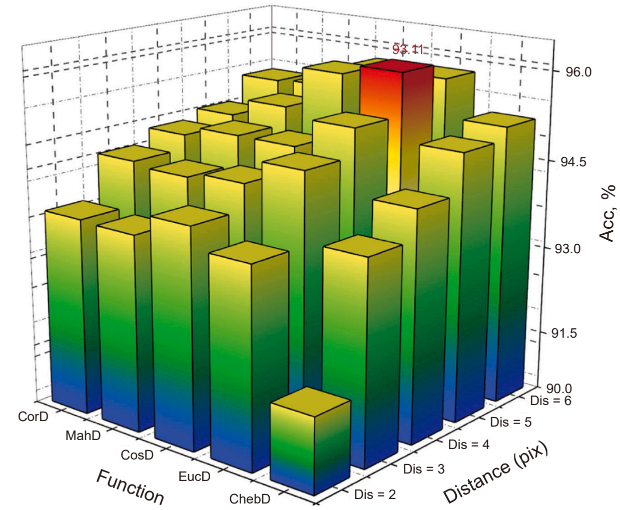

Fig. 12. Comparative results of distance constraint with different range and functions

coordinate distance (CorD) were systematically tested. The constraint on the receptive field range of neighboring nodes was varied from Dis = 2 to Dis = 6, generating 25 experimental configurations. For each configuration, the task performance was evaluated by averaging the accuracy (%) over 10 independent trials. The experimental results, summarized in Fig. 12, provide quantitative insights into the interplay between distance metric selection, neighborhood scope, and fault identification robustness.

As demonstrated in Fig. 12, the proposed model achieved its peak task performance, Acc = 93.11% under the EucD metric with a constraint range of Dis = 5, while the ChebD combined with Dis = 2 yielded the lowest accuracy Acc = 88.67%. A clear performance trend emerged: accuracy improved progressively as dis increased from 2 to 5, but this growth plateaued and even slightly declined when dis was further extended to 6. This phenomenon can be attributed to the expanded receptive field of neighboring nodes at larger dis values, which introduces redundant connections between sparsely intersecting fault blocks. Such over-connection reduces the signal-to-noise ratio (SNR) and amplifies computational overhead, thereby compromising both model robustness and temporal efficiency. Regarding distance metrics, the Euclidean distance consistently outperformed other functions, achieving superior alignment with the structured spatial patterns inherent to seismic images. The cosine distance ranked second, as its angular similarity measurement effectively captured directional fault trends—a critical feature for seismic fault identification. While alternative metrics (Chebyshev, Mahalanobis, and coordinate distances) remained functional, their suboptimal performance underscores the importance of selecting geometrically appropriate distance functions for fault system characterization.

5.2.2. Knowledge causally embedding

To balance information richness and computational efficiency while suppressing extraneous noise, establishing an optimal edge connection threshold Thr_ε is critical. To this end, the model's task performance was evaluated across varying thresholds using 10 key 2D seismic volume images. Performance variations observed in four critical main survey line profiles (illustrated in Figs. 5 and 6) and the aggregated evaluation metrics across all images are systematically presented in Fig. 13.

As depicted in Fig. 13, the Mean_Acc histogram exhibits a non-linear response to Thr_ε variations: accuracy increases from 91% at $Thr_\varepsilon = 0.5$ to a peak of 93.1% at $Thr_\varepsilon = 0.85$ followed by a gradual

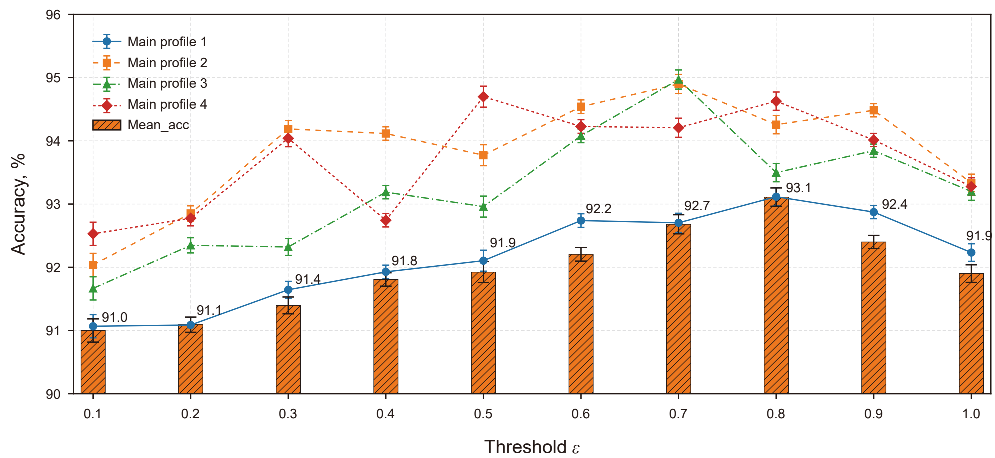

Fig. 13. Influences of different selection of fusion threshold parameter Thr_{ε}

decline to 92.4% and 91.9% at higher thresholds. The dotted line representing “Main Profile 1” strictly adheres to this unimodal pattern, achieving monotonic growth to its maximum before a controlled descent. While the three remaining profiles broadly align with this trend, their trajectories display localized deviations—specifically, non-positive initial slopes with intermittent performance dips prior to subsequent recovery and eventual improvement. Critically, the error bars across all results, with ranging between 0.1% and 0.3%, underscore the proposed method's operational stability, as performance fluctuations remain statistically constrained despite heterogeneous seismic volume characteristics (e.g., varying fault densities, azimuthal complexities) and spatially divergent fault properties. These minor deviations further validate the robustness of the edge connection thresholding mechanism in mitigating context-dependent noise.

5.3. *Influence of graph representation learning*

Beyond the effective incorporation of geological prior knowledge, the quality of graph representation learning serves as a critical determinant of task performance. This encompasses both the structural integrity of the Causally chained-graphs, governed by graph construction methodologies, and the model efficacy of graph neural network (GNN)-based learning frameworks. To systematically evaluate these factors, this subsection will experimentally validate and comparatively discuss the core methodologies and parameters underpinning graph representation learning.

5.3.1. *Graph qualities*

To assess the influences of graph construction methods, six graph types—sequential, fully-connected, and K-nearest neighbor (KNN) graphs (k = 2–5)—are evaluated using 100 graphs (900 nodes each correspond to original seismic image with size 30°×°30) trained for 100 epochs, with performance averaged over ten independent runs. Computational extremes are defined by the sequential graph (minimal adjacency) and fully-connected graph (dense edges), while intermediate connectivity is probed through KNN variants (k = 2–5). Identical model architectures, hyperparameters, and optimization protocols are maintained to isolate structural effects. Training durations per epoch are recorded to quantify computational costs, the key parameters of different graph construction method are listed in Table 4, and the performances of graphs are shown in Fig. 14.

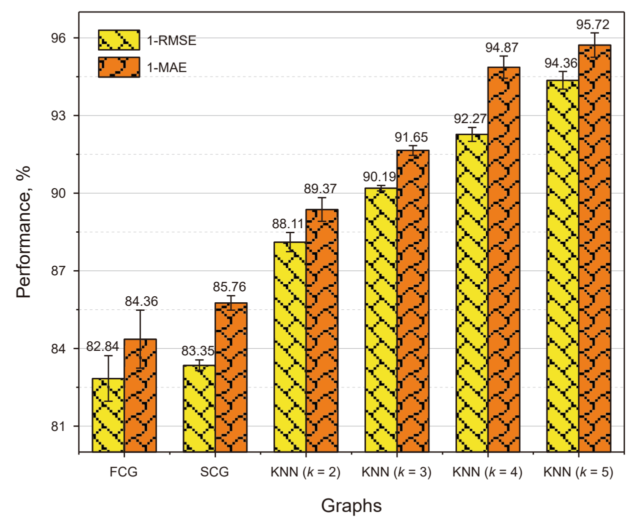

Fig. 14. Influences of different graph construction methods

Table 4
Key parameters of different graph construction method

No.	Graphs	Number of edges	Time, s		
			Graph construction	Training	Total time
1	FCG	404, 550	50.42	18.65	69.07
2	SCG	899	1.05	2.78	3.83
3	KNNG ($k = 2$)	756	10.67	3.52	14.19
4	KNNG ($k = 3$)	1173	23.46	4.77	28.23
5	KNNG ($k = 4$)	1615	32.91	5.83	38.74
6	KNNG ($k = 5$)	2074	42.77	7.54	50.31

The experimental results demonstrate substantial performance and computational trade-offs across graph construction methods, emphasizing the critical role of structural connectivity in balancing model efficacy and efficiency. As summarized in Table 4 and illustrated in Fig. 14, the fully-connected graph (FCG) achieves the highest performance, with 1-RMSE and 1-MAE values of 94.36% and 95.72%, respectively. However, this comes at a significant computational cost: FCG requires 404,550 edges, demanding 50.42 s for graph construction and 18.65 s per training epoch, resulting in a total runtime of 69.07 s. In contrast, the sequential graph (SCG), with only 899 edges, exhibits the lowest computational overhead (1.05 s for construction, 2.78 s for training, total 3.83 s) but delivers poor performance (1-RMSE: 82.84%, 1-MAE: 84.36%), highlighting the limitations of overly sparse connectivity.

KNN-based graphs (KNNG) interpolate between these extremes. Increasing the neighborhood size k from 2 to 5 enhances model performance (1-RMSE: 88.11% to 94.36%; 1-MAE: 89.37% to 95.72%) while progressively increasing computational demands. For instance, KNNG ($k = 5$) requires 2074 edges, incurring 42.77 s for graph construction and 7.54 s per training epoch (total 50.31 s). This represents a 27.2% reduction in total runtime compared to FCG, with only marginal performance degradation (1-RMSE: 94.36% vs. FCG's 94.36%; 1-MAE: 95.72% vs. FCG's 95.72%). Notably, KNNG ($k = 5$) achieves near-optimal accuracy while maintaining practical scalability, as its edge count and runtime scale linearly with k, unlike FCG's quadratic complexity. The sequential graph's poor performance underscores the necessity of sufficient connectivity for capturing global dependencies in seismic data. While FCG maximizes information flow, its prohibitive computational cost renders it impractical for large-scale applications. KNNG ($k = 5$) emerges as a balanced solution, offering 95.7% of FCG's performance at 72.8% of its runtime efficiency. These results emphasize the importance of tailoring graph topology to domain-specific constraints, prioritizing dense local connectivity (*via* KNNG) to approximate global interactions without exhaustive edge enumeration. For seismic image reconstruction, where both spatial correlation and computational feasibility are critical, KNNG ($k = 5$) provides an optimal trade-off between structural expressiveness and resource efficiency.

5.3.2. Graph learning model

To systematically evaluate how Chebyshev polynomial order K (varied from 2 to 7) governs the trade-off between model accuracy, computational efficiency, and training stability, each configuration was independently executed ten times under identical hyperparameters and initialization protocols. To ensure rigorous evaluation of convergence and prevent overfitting, we implemented an early stopping criterion with a patience of 50 epochs based on validation loss, while setting 1000 epochs as a sufficiently large upper bound that was never reached in practice. This repeated-measures design serves two critical purposes: (1) statistical robustness—by aggregating metrics (mean accuracy, 1-MAE, training time) across trials, we mitigate noise from stochastic optimization and weight initialization, distinguishing true model capacity from random fluctuations; (2) sensitivity analysis—recording variance in performance quantifies how sensitive the architecture is to minor receptive field adjustments. The isolation of K as the sole variable, with other hyperparameters fixed, ensures that observed differences directly reflect the impact of polynomial order on feature propagation in graph neural networks. Results are shown in Fig. 15 and Table 5.

Table 5
Experimental results in the different order K of Chebyshev convolution kernel

Value of K	Key performance		Value of K	Key performance	
	1-MAE, %	Time, s		1-MAE, %	Time, s
2	91.75 ± 0.81	12.36	5	95.84 ± 0.57	37.44
3	93.28 ± 0.63	19.18	6	94.76 ± 0.82	50.03
4	96.16 ± 0.46	28.56	7	94.35 ± 0.85	62.81

The relationship between Chebyshev order K, model capacity, and graph structural learning is systematically revealed through training dynamics and performance metrics in Fig. 15 and Table 5. When K is set to 2, the shallow receptive field restricts the model to aggregating information only from 1-hop neighborhoods, similar to traditional graph convolutional networks. This localized feature propagation fails to capture higher-order dependencies such as community structures or global topological patterns, resulting in an early plateau of the training loss curve and suboptimal performance with a mean absolute error of 8.25%. The underfitting phenomenon arises because node representations lack global context, leading to indistinguishable embeddings for structurally similar but distant nodes. In contrast, when K increases to 4, the model achieves an optimal balance between breadth and specificity. The 4-hop neighborhood aggregation enables multi-scale feature fusion: initial layers extract local patterns such as node attributes, while deeper layers integrate community-level semantics. This hierarchical fusion drives a smooth and monotonic decline in the training loss curve and achieves peak

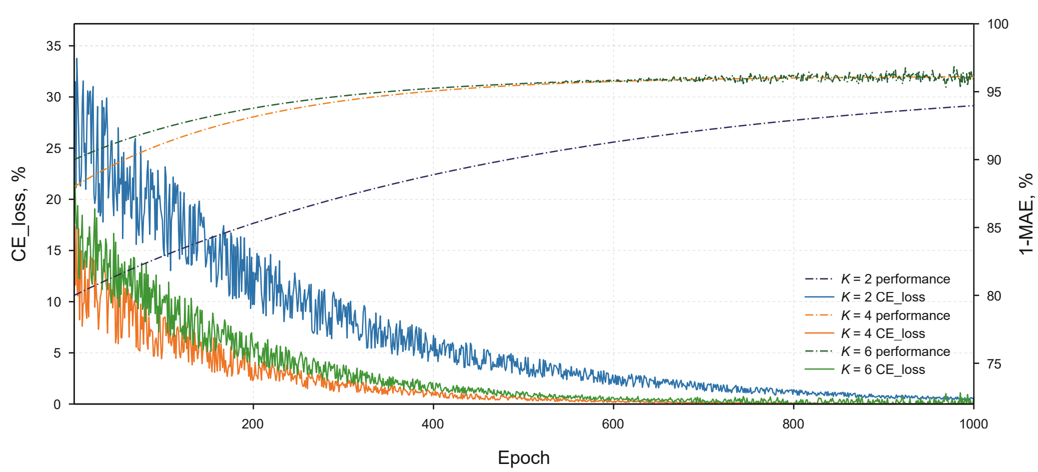

Fig. 15. Curves of model train in different key parameters

performance with a 1-MAE score of 96.16%. More importantly, both training and validation curves show stable convergence with minimal gap, demonstrating effective learning without overfitting. The model preserves discriminative features, such as bridge nodes or cluster boundaries, without over-smoothing, thereby maintaining class separability.

However, excessively increasing K beyond 5 introduces a phenomenon termed receptive field overreach. Although expanding the aggregation scope theoretically allows capturing broader graph structures, distant nodes—for example, those 6 hops away when K is 6—introduce irrelevant or adversarial signals, particularly in heterophilic graphs where neighboring nodes may belong to different classes. As shown in Fig. 15, the performance curve for K equal to 6 peaks early and then declines sharply, indicating that homogenized features erode class separability. This aligns with the oscillatory behavior of the loss curve after convergence, a hallmark of overfitting to noisy long-range connections. Critically, for $K = 6$ and $K = 7$, we observe the characteristic divergence where validation loss increases while training loss continues to decrease - a clear indicator of overfitting that was reliably captured within our training framework. Table 5 further quantifies the U-shaped trade-off between accuracy and computational complexity. The mean absolute error improves from 8.25% at K equals 2 to 3.84% at K equals 4, then deteriorates to 5.16% at K equals 7. Meanwhile, computational costs escalate nonlinearly with K; training time per epoch for K equals 4 is 2.1 times longer than for K equals 2, and K equals 7 triples the runtime while yielding only marginal initial performance gains. Notably, K equals 3 emerges as a pragmatic compromise, achieving 93.28% 1-MAE with 33% faster training than K equals 4. This highlights the critical trade-off between accuracy, which peaks at K equals 4, and efficiency, which is optimal at K equals 2.

The variance metrics further validate these trends. The minimal variance of ± 0.46 at K equals 4 underscores its stability, whereas higher K values amplify optimization uncertainty, as seen in the ± 0.85 variance for K equals 7. This instability stems from conflicting gradient updates caused by aggregating features from disparate neighborhoods. The training adequacy is further supported by the fact that all configurations reached stable convergence points, with the optimal $K = 4$ achieving both the best performance and lowest variance across multiple runs. These findings emphasize a Goldilocks principle for selecting K: the optimal order should neither be too localized nor excessively global, but instead contextually aligned with graph density, task semantics, and resource constraints. For instance, in sparse graphs or tasks requiring fine-grained community detection, moderate K values like 3 or 4 are preferable, while small K may suffice for resource-constrained applications prioritizing inference speed over precision.

6. Conclusion

Current fault identification methods for gas storage safety often suffer from insufficient integration of geological causality, particularly in capturing physical mechanisms and addressing subsurface confounders, which restricts their sensitivity to subtle seismic signatures. To address this, we developed a multi-knowledge causally embedded graph representation approach that transforms seismic interpretation into node classification constrained by geological priors. The methodology uniquely constructs Causally chain-graphs through knowledge-driven edge optimization, where fault continuity and seismic patterns are explicitly encoded as causal relationships, enabling graph convolutions to propagate features across non-Euclidean neighborhoods while preserving geological consistency. Validation in a Central China gas storage site including regional, block-bounding, and minor intra-block faults demonstrated robust performance, with 93.11% accuracy and a 0.758 F1-score, significantly improving detection of subtle faults exhibiting less than 5% amplitude variation. This approach offers a causally interpretable tool for assessing critical risks including tectonic reactivation and caprock integrity.

However, the proposed method mainly focuses on the accurate identification of discontinuous faults from the geological background given by the existing seismic signals, and there is no further explanation of the formation structure based on the identified faults. How to construct the whole process model of seismic signal processing, fault identification and geological interpretation is the research target of the next stage.

CRediT authorship contribution statement

Feng-Yuan Zhang: Writing – original draft, Methodology, Investigation. **Ji-Zhou Tang:** Writing – review & editing, Funding acquisition, Conceptualization. **Hong-Liang Wu:** Supervision, Resources. **Jie Liu:** Writing – review & editing, Methodology, Investigation. **Jun Zhou:** Project administration. **Shi-Jie Zhao:** Writing – original draft, Validation, Methodology. **Fa-Mu Huang:** Resources, Investigation. **Juan Zhang:** Visualization, Validation, Supervision. **Hao Wang:** Methodology. **Jun-Lun Li:** Formal analysis, Data curation.

Declaration of competing interest

The authors declare that they have no known competing financial interests or personal relationships that could have appeared to influence the work reported in this paper.

Acknowledgements

The authors would like to thank China Oil & Gas Pipeline Network Corporation for providing the field dataset in this study. This work was also supported by the National Natural Science Foundation of China (No. U24B2034), the Shanghai Rising-Star Program (No. 24QA2709700), and the National Science and Technology Major Projects of China (No. 2025ZD1401107).

References

Bomfim, L., Cunha, O., Kuroda, M., et al., 2023. Transformer model for fault detection from Brazilian pre-salt seismic data. In: Brazilian Conference on Intelligent Systems. Springer, Nature Switzerland, Cham, pp. 3–17. https://doi.org/10.1007/978-3-031-45389-2_1.

Botter, C., Cardozo, N., Hardy, S., et al., 2014. From mechanical modeling to seismic imaging of faults: a synthetic workflow to study the impact of faults on seismic. Mar. Petrol. Geol. 57, 187–207. https://doi.org/10.1016/j.marpetgeo.2014.05.013.

Chen, T., Kornblith, S., Norouzi, M., et al., 2020. A simple framework for contrastive learning of visual representations. In: International Conference on Machine Learning. PMLR, pp. 1597–1607. https://doi.org/10.48550/arXiv.2002.05709.

Choi, Y., Jo, Y., Seol, S.J., et al., 2021. Deep learning spectral enhancement considering features of seismic field data. Geophysics 86 (5), V389–V408. https://doi.org/10.1190/geo2020-0017.1.

Di, H., Shafiq, M.A., AlRegib, G., 2017. Seismic-fault detection based on multi attribute support vector machine analysis. In: SEG International Exposition and Annual Meeting. SEG, pp. 2128–2132. https://doi.org/10.1190/segam2017-17748277.1.

Di, H., Shafiq, M.A., Wang, Z., et al., 2019. Improving seismic fault detection by super-attribute-based classification. Interpretation 7 (3), SE251–SE267. https://doi.org/10.1190/INT-2018-0188.1.

Etgen, J., Gray, S.H., Zhang, Y., 2009. An overview of depth imaging in exploration geophysics. Geophysics 74 (6), WCA5–WCA17. https://doi.org/10.1190/1.3223188.

Faleide, T.S., Braathen, A., Lecomte, I., et al., 2021. Impacts of seismic resolution on fault interpretation: insights from seismic modelling. Tectonophysics 816, 229008. https://doi.org/10.1016/j.tecto.2021.229008.

Freeman, B., Boult, P.J., Yielding, G., et al., 2010. Using empirical geological rules to reduce structural uncertainty in seismic interpretation of faults. J. Struct. Geol. 32 (11), 1668–1676. https://doi.org/10.1016/j.jsg.2009.11.001.

Geng, Z., Liu, J., Li, S., et al., 2023. Channel attention-based static-dynamic graph convolutional network for lithology identification with scarce labels. Geoenergy Sci. Eng. 223, 211526. https://doi.org/10.1016/j.geoen.2023.211526.

Griffiths, D.H., King, R.F., 2013. Applied Geophysics for Geologists and Engineers: the Elements of Geophysical Prospecting. Pergamon Press, Oxford. https://doi.org/10.1016/C2009-0-10955-8.

Guitton, A., Wang, H., Trainor-Guitton, W., 2017. Statistical imaging of faults in 3D seismic volumes using a machine learning approach. In: SEG Technical Program Expanded Abstracts. Society of Exploration Geophysicists, pp. 2045–2049. https://doi.org/10.1190/segam2017-17589633.1.

Jaiswal, K.K., Chowdhury, C.R., Yadav, D., et al., 2022. Renewable and sustainable clean energy development and impact on social, economic, and environmental health. Energy Nexus 7, 100118. https://doi.org/10.1016/j.nexus.2022.100118.

Johansson, M., 1999. The Hilbert Transform. Mathematics Master's Thesis. Växjö University, Sweden. Available at: http://w3.msi.vxu.se/exarb/mj_ex.pdf. (Accessed 19 October 2024).

Li, P., Li, Y., Shi, X., et al., 2021. Stability analysis of U-shaped horizontal salt cavern for underground natural gas storage. J. Energy Storage 38, 102541. https://doi.org/10.1016/j.est.2021.102541.

Li, X., Li, K., Xu, Z., et al., 2023a. Fault-Seg-Net: a method for seismic fault segmentation based on multi-scale feature fusion with imbalanced classification. Comput. Geotech. 158, 105412. https://doi.org/10.1016/j.compgeo.2023.105412.

Li, X., Sun, L., Ling, M., et al., 2023b. A survey of graph neural network based recommendation in social networks. Neurocomputing 549, 126441. https://doi.org/10.1016/j.neucom.2023.126441.

Lin, L., Zhong, Z., Cai, Z., Sun, A.Y., Li, C., 2022. Automatic geologic fault identification from seismic data using 2.5D channel attention U-Net. Geophysics 87, IM111–IM124. https://doi.org/10.1190/geo2021-0805.

Lin, L., Zhong, Z., Li, C., et al., 2024. Machine learning for subsurface geological feature identification from seismic data: methods, datasets, challenges, and opportunities. Earth Sci. Rev. 253, 104887. https://doi.org/10.1016/j.earscirev.2024.104887.

Liu, Z., Deng, Z., He, G., et al., 2022. Challenges and opportunities for carbon neutrality in China. Nat. Rev. Earth Environ. 3 (2), 141–155. https://doi.org/10.1038/s43017-021-00244-x.

Lu, G., Zeng, L., Liu, G., et al., 2024. Fracture Identification based on graph pooling and graph construction in continental shale. IEEE Trans. Geosci. Rem. Sens. 62, 1–15. https://doi.org/10.1109/TGRS.2024.3385594.

Shaw, J.H., Connors, C., Suppe, J., 2005. Seismic Interpretation of Contractional Fault-Related Folds. American Association of Petroleum Geologists, Tulsa. https://doi.org/10.1306/St531003.

Song, T., Zheng, W., Song, P., et al., 2018. EEG emotion recognition using dynamical graph convolutional neural networks. IEEE Trans. Affect. Comput. 11 (3), 532–541. https://doi.org/10.1109/TAFFC.2018.2817622.

Sun, Z., Yin, H., Chen, H., et al., 2020. Disease prediction *via* graph neural networks. IEEE J. Biomed. Health Inform. 25 (3), 818–826. https://doi.org/10.1109/JBHI.2020.2984705.

Tang, J., Li, J., Zhang, Z., et al., 2025. Differential impacts of multi-scale natural fractures on hydraulic fracture network formation. Earth Sci. Rev. 257, 105315. https://doi.org/10.1016/j.earscirev.2024.105315.

Tang, Z., Wu, B., Wu, W., et al., 2023. Fault detection *via* 2.5 d transformer u-net with seismic data pre-processing. Remote Sens. 15 (4), 1039. https://doi.org/10.3390/rs15041039.

Tian, F., Zhang, J., Zheng, W., et al., 2023. "Geology-geophysics-data mining" integration to enhance the identification of deep fault-controlled paleokarst reservoirs in the Tarim Basin. Mar. Petrol. Geol. 158, 106498. https://doi.org/10.1016/j.marpetgeo.2023.106498.

Wang, H., Zhao, M., Xie, X., et al., 2019. Knowledge graph convolutional networks for recommender systems. In: The World Wide Web Conference. ACM, San Francisco, pp. 3307–3313. https://doi.org/10.1145/3308558.3313417.

Wang, X., Li, Z., Li, W., et al., 2025. Study on gas migration through cement microstructure under multi-field effects during offshore gas storage well construction. Constr. Build. Mater. 460, 139846. https://doi.org/10.1016/j.conbuildmat.2024.139846.

Wang, Z., You, J., Liu, W., et al., 2023. Transformer assisted dual U-net for seismic fault detection. Front. Earth Sci. 11, 1047626. https://doi.org/10.3389/feart.2023.1047626.

Wu, X., Liang, L., Shi, Y., et al., 2019. FaultSeg3D: using synthetic data sets to train an end-to-end convolutional neural network for 3D seismic fault segmentation. Geophysics 84 (3), IM35–IM45. https://doi.org/10.1190/geo2018-0646.1.

Xiong, W., Ji, X., Ma, Y., et al., 2018. Seismic fault detection with convolutional neural network. Geophysics 83 (5), O97–O103. https://doi.org/10.1190/geo2017-0666.1.

Yang, C., Liu, J., Xu, Q., et al., 2023. A generalized graph contrastive learning framework for few-shot machine fault diagnosis. IEEE Trans. Ind. Inf. 20 (2), 2692–2701. https://doi.org/10.1109/TII.2023.3297664.

Zhang, F., Liu, J., Liu, Y., et al., 2024a. Data-model-interactive enhancement-based Francis turbine unit health condition assessment using graph driven health benchmark model. Expert Syst. Appl. 249, 123724. https://doi.org/10.1016/j.eswa.2024.123724.

Zhang, F., Liu, J., Liu, Y., et al., 2025a. Heterogeneous graph contrastive learning-based transductive health condition assessment of Francis turbine unit. Eng. Appl. Artif. Intell. 145, 110240. https://doi.org/10.1016/j.engappai.2025.110240.

Zhang, F., Tang, J., Zhou, J., et al., 2026. Securing CO_2 storage in fractured reservoirs: intelligent characterization of critical natural fracture pathways. Fuel 406, 136915. https://doi.org/10.1016/j.fuel.2025.136915.

Zhang, M., Tang, J., Meng, S., et al., 2025b. Research on the storage performance evaluation and economic prediction of catalyzed Green Methanol Underground. Appl. Energy 404, 126779. https://doi.org/10.1016/j.apenergy.2025.126779.

Zhang, S., Tong, H., Xu, J., et al., 2019. Graph convolutional networks: a comprehensive review. Computational Social Networks 6 (1), 1–23. https://doi.org/10.1186/s40649-019-0069-y.

Zhang, Z., Tang, J., Fan, B., et al., 2024b. An intelligent lithology recognition system for continental shale by using digital coring images and convolutional neural networks. Geoenergy Sci. Eng. 239, 212909. https://doi.org/10.1016/j.geoen.2024.212909.

Zhao, S., Ding, R., Han, T., Liu, Y., Zhang, J., Zhao, L., 2023. Fault2SeisGAN: A method for the expansion of fault datasets based on generative adversarial networks. Frontiers in Earth Science 11, 1091803. https://doi.org/10.3389/feart.2023.1091803.